Assessment of Reynolds-Averaged Navier–Stokes/Blade Element Theory Body Force Method for Propeller Modeling

Hugues Pantel, Fabrice Falissard, Guillaume Dufour

Assessment of Reynolds-Averaged Navier–Stokes/Blade Element Theory Body Force Method for Propeller Modeling

Hugues Pantel* and Fabrice Falissard†
DAAA, ONERA, Paris-Saclay University, F-92190 Meudon, France

Guillaume Dufour‡
ISAE-SUPAERO, Toulouse University, F-31055 Toulouse, France

This work presents an actuator disk-like body force method designed for propeller modeling, which is based on a full coupling between Computational Fluid Dynamics (CFD) and Blade Element Theory (BET). An analysis is conducted on the model to identify best practices for source term distribution. It is found that the source term volume shape has no impact on propeller loads and flow field, and that the velocities used for the BET analysis at each radial section should be evaluated exactly where half the source terms have been distributed in the CFD domain. Four tip-loss corrections, including two from literature, are also analyzed and compared to lifting-line and RANS blade-resolved computations. The best practices and the most effective tip-loss correction lead to a final model that is compared to lifting-line, RANS and URANS computations for different pitch angles and incidence angles, on the ONERA HAD-1 three-bladed light propeller. The RANS/BET body force model predicts thrust within 3% for axial flow and 8% for cases with incidence. The same accuracy is obtained for wake prediction.

Presented as Paper 2023-3668 at the AIAA AVIATION 2023 Forum, San Diego, CA, 12-16 June 2023.
*Ph.D. Student, Department of Aerodynamics, Aeroelasticity, and Acoustics.
†Research Scientist, Ph.D., Department of Aerodynamics, Aeroelasticity, and Acoustics, fabrice.falissard@onera.fr (Corresponding author).
‡Associate Professor, Ph.D., Department of Aerodynamics, Energy and Propulsion.

Nomenclature

c = chord, m

C_P = power coefficient, $P/\rho\, n^3 (2R)^5$

C_T = thrust coefficient, $T/\rho\, n^2 (2R)^4$

D = drag force, N

L = lift force, N

M = Mach number

n = rotation frequency, Hz

N_b = number of blades

N_i = number of cells in radial direction

N_j = number of cells in azimuthal direction

N_k = number of cells in axial direction

P = power, W

R = propeller radius, m

r = radial coordinate, m

R_e = Reynolds number

T = thrust, N

V_x = axial velocity, m.s^{-1}

V_t = tangential velocity in rotor plane, m.s^{-1}

V_0 = norm of free flow velocity, m.s^{-1}

V_{rel} = velocity relative to propeller section, m.s^{-1}

x = axial coordinate, m

α = angle of attack, deg

β = pitch angle, deg

θ = tangential angle coordinate, rad

Θ = incidence angle, deg

ρ = density, kg.m^{-3}

ϕ = local flow angle, deg

Ψ = azimuth angle, deg

Ω = rotation speed in rad.s^{-1}

I. Introduction

Propeller and rotor studies have surged in recent years thanks to the research and development of compound helicopters, aircraft with distributed propulsion, Urban Air Mobility (UAM) for public transportation, and to the continuous effort to develop high-speed open rotors for commercial aviation. Compound helicopters and UAM concepts often exhibit multiple rotors mounted on hubs or wings, such that installation effects and mutual rotor aerodynamic interactions have a first order impact on the flight physics and aerodynamic performance of the vehicle. These effects must then be taken into account for security and aircraft performance assessment. For commercial aviation, the challenge is to design an aircraft that is competitive compared to turbofan-powered aircraft. The aerodynamic performance of both the engine and airframe must therefore be carefully evaluated together to assess the benefits of the overall architecture.

State of the art Computational Fluid Dynamics (CFD) is able to provide such an assessment but at a cost in manpower and computational resources that is not affordable in preliminary studies. On the other side of the spectrum of methods available for propeller assessment are codes based on the Blade Element Momentum Theory (BEMT) [1] and the

lifting-line theory [2]. These are very fast and accurate methods for computing isolated rotor performance but they lose in accuracy when trying to account for strong installation effects. This is why methods developed to assess the performance of aircraft with propellers or open rotors often rely on hybrid Navier-Stokes approaches. These use CFD-RANS to model the flow fields, a lower fidelity method to model the propeller, and a coupling between the two. Because there is no body-fitted blade mesh, this approach can offer a significant gain in mesh size, and thus reduce computational costs. This paper will only focus on fully coupled methods, as a retro-action of the flow on the propeller loading is of first importance when studying strong installation effects. Hybrid Navier-Stokes approaches can be either time-accurate by modeling the distinct rotating blades [3], or time-averaged by averaging the propeller effect on the flow over a whole revolution. Because time-averaged methods only predict the mean flow, they only give partial information on installation effect studies. However, they make it possible to conduct steady simulations where blade-resolved analyses of installation effects require unsteady computations, thus lowering computation costs further. Time-accurate hybrid Navier-Stokes methods for propeller modeling will be investigated in future work, and this paper will only focus on time-averaged methods. For helicopter, wind turbine, and propeller applications, blade loads are often computed using the Blade Element Theory, which is well suited for hybrid Navier-Stokes computations because it takes the local velocity fields as inputs and returns local loads.

The effect of the propeller can be included in the CFD computation in two ways. The first method is to use internal boundary conditions in the computational mesh. Fejtek and Roberts [4] link propeller thrust to a pressure jump, and propeller torque to a flow deviation on a helicopter application. These two conditions are applied at the rotor disk, which must conform to the computational grid. Moens and Gardarein [5] use the same type of conditions to model interactions between a propeller and a wing, but use maps of lifting-line results to compute blade loads. The second method to include propeller or rotor effect into CFD-RANS computations is to use source terms in the Navier-Stokes equations. This was first done by Rajagopalan and Lim [6] who coupled 2D Navier-Stokes with BET to model a helicopter rotor in hover. Rajagopalan and Mathur [7] extend this to 3D Navier-Stokes to model a helicopter in forward flight. Zori and Rajagopalan [8] study interaction effects between a helicopter rotor and a fuselage. These authors do not explicitly explain how the source terms are distributed inside the CFD mesh. Sørensen and Miken [9] distribute them in a one cell thick volume using a Dirac function. Sørensen et al. [10] project the source terms using a convolution product with a 3D Gaussian kernel. This is done to avoid instabilities that appear when the source term volume is only one cell thick. The 3D Gaussian kernel is still widely used today [11, 12], but it spreads the distribution of source terms at radii greater than the rotor radius, and leads to a distortion of the spanwise loads. As a result, a 1D Gaussian is now also used to only distribute the source terms in the axial direction [13, 14]. The source term distribution methods presented above were used to avoid numerical instabilities. Ortun [15] uses an axial distribution law to better reproduce real blade physics by concentrating the majority of the source terms toward the front of the volume. The sources are furthermore only distributed in the area swept by the blades. This method was used to study installation effects of a propeller on a wing.

The same setup is used by Reboul et al. [16] for aeroacoustic predictions of an eVTOL rotor. However because these various methods have been applied on different cases, there is no consensus in the scientific community as to what the best practices are for source-term distribution. The different distribution methods have yet to be tested on a unique application case.

The modeling methods presented above average the propeller loads on a full revolution and thus only give a time-averaged prediction of the velocity fields. As a result, the blade-tip vortices are not captured, so the methods require tip loss corrections for the same reasons as in the BEMT. Prandtl initially used vortex theory to propose a correction factor to Betz's optimal propeller design [17] to extend its validity from an infinite to a finite number of blades. Glauert [1] then suggests a modification to Prandtl's theory for a simple implementation in the BEMT. This modified version can be seen as a correction of the induced velocities to virtually account for tip vortices. The formulation derived by Glauert is nowadays still widely used and some refinement proposals were made, for example to correct mass flow [18, 19] or to account for the possible azimuthal dependency of the correction [20]. Shen et al. [21] make an extensive analysis of the coherency of the Glauert tip loss and find in particular that it implicitly assumes zero C_l and zero flow angle at the tip, which is not realistic for cambered airfoils. The authors thus propose for the BEMT a variant to Glauert's tip loss factor that better models the physics at the very tip of the blade.

All these methods were developed for BEMT, and the way they should be included in a Navier-Stokes and BET coupling is not clear. Sørensen and Kock [22] initially applied Glauert's correction factor by multiplying it to the interpolated section's lift coefficient. Shen et al. [23] proposed an iterative method that uses Glauert's factor to correct the sampled velocities before computing the loads with BET. They also correct the BET loads by a factor that brings the loads down to zero at the very tip of the blade to account for 3D effects. Zhong et al. [14] attempt a review of the existing tip loss corrections that exist for Navier-Stokes and BET couplings. However, these corrections were tested on wind turbine applications and the conclusions are not necessarily directly valid for propeller applications.

The propeller modeling method presented in this paper is a steady three-dimensional RANS/BET coupling method. The approach is detailed and applied to an isolated three-bladed light propeller. A thorough investigation into the distribution methods of the source terms into the CFD mesh is conducted. A focus is made on the different possible parameterizations of the source terms and on their effects on both the propeller's aerodynamic performance and the structure of its wake, which is of first importance if it impinges on a lifting surface placed downstream. Four tip-loss corrections are also compared. The model is evaluated on a range of propeller pitch angles in axial flow as well as on different incidence angles. Detailed comparisons are shown between results obtained by RANS blade-resolved, lifting-line theory and RANS/BET methods.

II. Propeller Geometry and Operating Point

The geometry studied in this paper is the ONERA HAD-1 propeller [15] shown in Fig. 1. It is a three-bladed light propeller designed according to the minimum induced loss method of Adkins and Liebeck [24], for a tip Mach number equal to 0.5, a 1.6 meter diameter and a propeller thrust representative of the cruise condition of a general aviation aircraft with two propellers. In addition, the blade chord distribution obtained with the Adkins and Liebeck method was smoothed with the parameterization proposed by Borer et al. [25]. The blade's chord and twist distributions are shown in Figure 2. The propeller's main characteristics, cruise operating point and performance are summarized in Tables 1 to 3. The reference radius for the blade pitch angle is chosen at 75% of the propeller's tip radius.

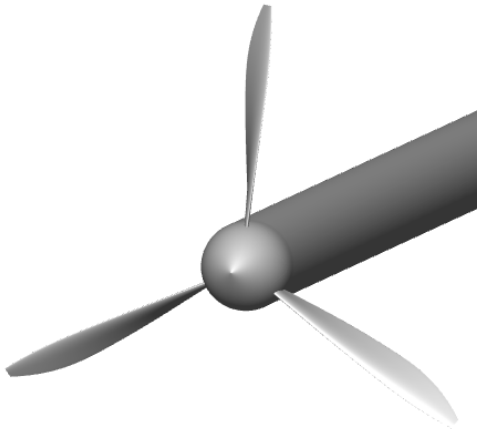

Fig. 1 HAD-1 propeller.

Table 1 HAD-1 propeller characteristics

Parameter	Value
Blade count, N_b	3
Tip radius [m]	0.8
Hub-to-tip ratio	0.15

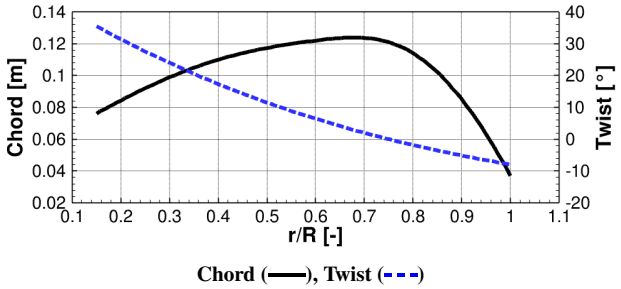

Fig. 2 Chord and twist distributions of HAD-1 blade.

Table 2 HAD-1 cruise operating point

Parameter	Value
Mach number, M_0	0.3
Angle of incidence [°]	0
Air temperature [K]	288.15
Air density [kg.m^{-3}]	1.225
Rotation speed [rad.s^{-1}]	212.7
Advance ratio	1.9
Blade pitch angle [°]	45

Table 3 HAD-1 performance at cruise operating point

Parameter	Value
Thrust [N]	1390
Power [kW]	164.4
Thrust coefficient, C_T	0.15
Power coefficient, C_P	0.33
Efficiency, η	0.863

III. Flow Modeling and Computational Methodologies

The RANS/BET body force method presented in this paper will be assessed by comparison of its results with blade-resolved CFD computations (RANS and URANS for unsteady cases) that are used as references. Lifting-line computations are also conducted using the same airfoil polars as for the RANS/BET approach. The lifting-line method models distinct blades whereas the RANS/BET approach distributes the loads on a full revolution and thus needs a tip-loss correction.

A. Blade-Resolved Approach

The Computational Fluid Dynamics (CFD) computations were performed with the elsA* finite-volume solver [26] using the Reynolds-Averaged Navier-Stokes (RANS) equations in compressible regime. For steady operating points at zero incidence, the simulations are carried out considering one blade channel only, using azimuthal periodic boundary conditions. The convective fluxes are discretized using a second-order centered scheme with scalar artificial viscosity [27] and Martinelli's correction [28]. The coefficients of the second-order nonlinear, fourth-order linear dissipation and Martinelli's scaling exponent are set, respectively, to $k^{(2)} = 1/2$, $k^{(4)} = 0.044$, and $\alpha = 0.33$. The diffusive fluxes are discretized using a second-order centered scheme and the turbulence modeling relies on a $k - \omega$ Kok turbulence model [29] with shear-stress transport (SST) correction [30] and limiters [31]. The computations are carried out considering an absolute velocity formulation within the relative reference frame. Characteristic relation-based flow boundary conditions are used at the computational domain inlet, outlet, and radial boundary with infinite flow values corresponding to the ones given in Tab. 2. All solid surfaces are considered as adiabatic walls using a low Reynolds approach. The pseudo time-marching scheme used for the steady computations is the first-order backward Euler scheme.

For operating points with incidence, the flow becomes unsteady and periodic boundary conditions can no longer be used. The mesh of the single blade channel is duplicated to obtain a full 360° mesh, and kinematic motion is applied to the grid in the absolute frame. The unsteady simulations are carried out using a second-order three-time-level implicit backward-difference scheme. The time-step was chosen so the propeller rotates half a degree at each iteration.

Five structured multiblock grids of a single blade channel were made using the NUMECA Autogrid mesh generation software. The number of cells in each grid is given in Table 4. The computational domain extends 6 radii upstream, 6 radii downstream of the rotor pitch axis and 6 radii in the radial direction. Slices of the mesh containing 10.1 million cells are represented in Figure 3. Each mesh was built so that the first-layer thickness complies with the y^+ requirement of the turbulence model of $y^+ \leq 1$.

A RANS simulation was conducted on each grid using the computational setup detailed above and the operating point from Table 2. The propeller thrust and power computed at the end of each simulation are shown in Table 4. These

*elsA V5.1.01 ONERA-Safran property

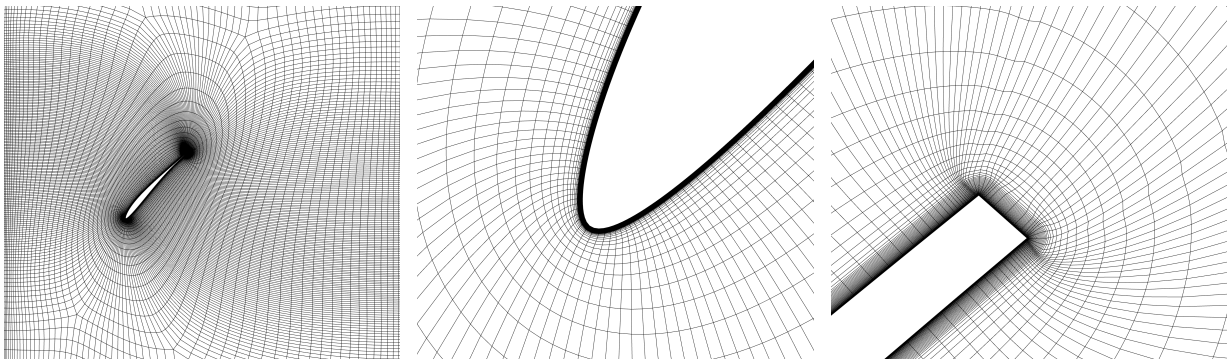

(a) Blade section mesh (b) Blade section mesh - leading edge (c) Blade section mesh - trailing edge

Fig. 3 Blade-resolved mesh used for RANS and URANS computations.

two quantities of interest are converged well below 1%. The radial distributions of blade thrust and tangential loads are represented on Figure 4 and are nearly identical for each mesh. The same is noted in Figures 5 and 6 for the azimuthal averages of velocity fields in the wake, which are of interest in the next sections to compare to RANS/BET results.

As a result, grid convergence is assumed sufficient for the RANS blade-resolved computations to be used as references for the comparisons with RANS/BET results. In the following, all blade-resolved results are obtained from Grid 4. This grid may be over-refined for the case presented in this grid-dependency study, but the extra refinement may be necessary for computations with higher pitch angles or for the study with incidence angles.

Table 4 Grid-dependency study results

Grid	Number of cells	Thrust [N]	Power [kW]
1	3,363,296	1393.1	165.08
2	5,065,824	1390.6	164.90
3	6,958,816	1392.5	164.87
4	10,132,608	1389.7	164.39
5	12,452,352	1389.7	164.37

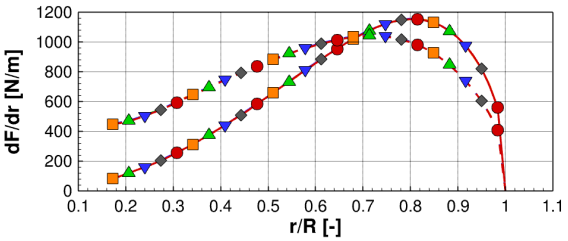

Grid 1 (—■—), 2 (—▲—), 3 (—▼—), 4 (—◆—), and 5 (—●—)

Fig. 4 Axial (solid) and tangential (dashed) loads for each grid.

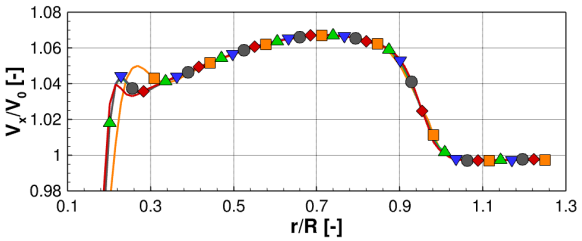

Grid 1 (—■—), 2 (—▲—), 3 (—▼—), 4 (—◆—), and 5 (—●—)

Fig. 5 Azimuthal average of axial velocity one radius behind the rotor for each grid.

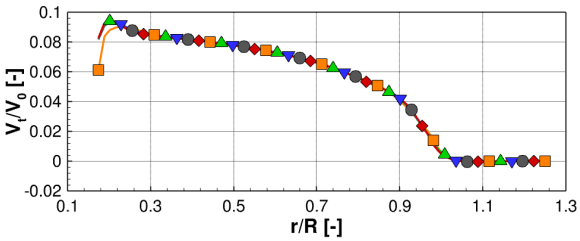

Grid 1 (—■—), 2 (—▲—), 3 (—▼—), 4 (—◆—), and 5 (—●—)

Fig. 6 Azimuthal average of tangential velocity one radius behind the rotor for each grid.

B. Lifting-Line Approach

The lifting-line calculations are performed with the PUMA solver (Potential Unsteady Methods for Aerodynamics), developed by ONERA. It relies on a coupling between a kinematic module and an aerodynamic module based on a free-wake model combined with a lifting-line approach. The lifting-line method relies on 2D airfoil polars (lift, drag, and moment coefficients) to compute the airloads on the blade sections. The free-wake model implements Mudry's theory [32], which rigorously describes the unsteady evolution of a wake modeled by a potential discontinuity surface. The PUMA code is parallelized using OpenMP and the multilevel Fast Multipole Method has been implemented for the computation of the velocities induced by each wake panel on any element. It is also able to take into account the non-lifting potential field of solid surfaces with arbitrary geometries. In recent years, it has been successfully applied and validated on fixed and rotating wings applications such as propellers [33], conventional and compound helicopters [34, 35], as well as wind turbines [36].

Figure 7 shows the free wake computed by PUMA for an HAD-1 simulation. PUMA can also be given a perturbation field to be included in the computations to account for the flow field around the spinner and hub. In the case studied here, this perturbation field is generated using the finite volumes CFD code described in section III.A.

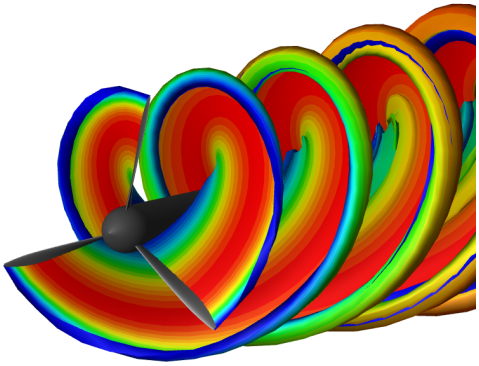

Fig. 7 Free wake of HAD-1 from PUMA colored by circulation.

Fig. 8 Blade sections chosen for airfoil polar computations.

For this study each blade was discretized in 35 sections by interpolation in HAD-1's geometric definition. The airfoil polars used by the lifting-line solver were computed for 6 blade sections using CFD, distributed as in Figure 8. For each section, 2D RANS computations were carried out for various Mach numbers and incidence angles, ranging respectively from 0.2 to 0.85, and from -8° to 12°. The airfoil polars were computed at the approximate Reynolds number seen by each section.

At the end of the computation, PUMA returns integrated aerodynamic performance as well as blade loading distribution and the 3D geometry of the wake and its circulation field. This data can be post-processed into a spatial velocity field, using the Biot-Savart law, and compared to the velocity fields computed with the RANS blade-resolved and RANS/BET approaches.

C. RANS/BET Approach

The RANS/BET approach presented in this paper models the propeller as distributed (volumic) source terms in a CFD RANS computation on a grid that does not include the blades mesh. For each azimuthal position, the local flow information at each radius is used to compute the section load with a BET approach, using the airfoil polars described above. The load is then axially distributed using a prescribed weighting function. This is done at each azimuthal point, such that the force is local (in the radial and azimuthal sense), thus making the approach able to model non-uniform inflow conditions (such as incidence or interaction effects).

The RANS/BET source term approach is formally similar to the Body Force Method (BFM) approaches used for internal turbomachinery flow (see refs. [37–40] for instance), in the sense that blades are represented by volumic source terms that can be viewed as forces acting on the flow. However, the methods differ in the underlying modeling principles: (i) for the RANS/BET approach, the starting point is to express the forces from isolated airfoils polars, whereas (ii) for turbomachinery BFM, the forces are expressed from the turning and the losses generated by a blade row.

Compared with classical blade-resolved approaches, the RANS/BET method offers a significant computational gain for non-uniform conditions: (i) the grid size is reduced because the blades are not meshed, and (ii) the modeled flow is steady because the method intrinsically smears out blade-to-blade effect, whereas a blade-resolved computation for a non-uniform inflow requires unsteady computations. This is done at the cost of certain hypotheses: because of the use of polars, the blades are assumed to be independent and with a 2D flow. Thus, blade-to-blade effects such as wakes or tip vortices are not present in the resulting flow field. In other words, the flow obtained by the RANS/BET can be seen as representative of the time-averaged flow over a full rotor revolution computed with a blade-resolved approach.

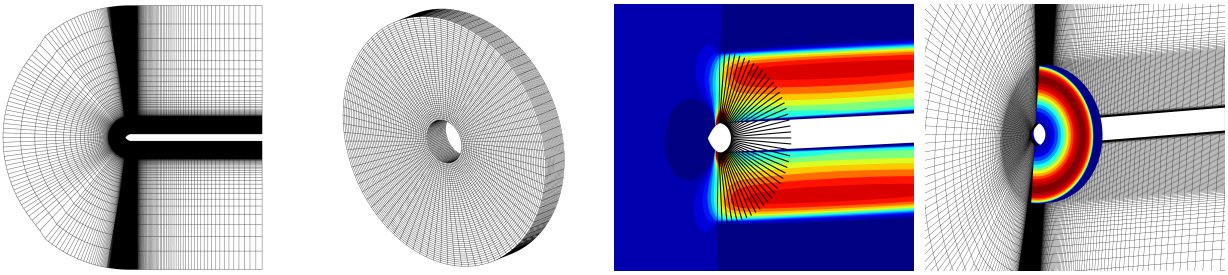

(a) Slice of CFD grid **(b) Source term volume** **(c) Velocity fields extraction** **(d) Source terms distribution**

Fig. 9 RANS/BET method recap.

1. Grids

Two distinct 3D grids are used in the RANS/BET method. The first one is the computational mesh used for the CFD RANS simulation, displayed in Figure 9a. It does not include a body-fitted blade mesh but may include any other object (propeller hub, wing, full aircraft). It must be refined where the source terms are applied. This can for example be done

with an overset grid when the mesh contains many different objects. In this study a curvilinear structured 3D mesh fitting the spinner prolonged by an infinite cylindrical hub is used. It is refined in the propeller and wake areas and is composed of 10 million cells for a 360 degree volume. It should be noted here that the whole annulus domain is only necessary for the final computations with an non-zero incidence on the propeller.

The second grid meshes the volume in which the source terms are distributed (Figure 9b). This auxiliary grid is only used to compute the source terms and is independent of the CFD calculation. The volume may have different shapes and the effect of this parameter is investigated in section IV.A. Regardless of the shape, the volume has N_i, N_j, and N_k nodes respectively in the radial, azimuthal and axial directions.

2. Propeller Loads Computation

As explained previously, the local load at a given radius and azimuth is computed using BET. To do so, the flow velocities needed for the computation are extracted from the CFD flow fields. This is done by interpolating the CFD solution on N_j sampling lines as displayed in Figure 9c. The sampling lines used in this paper are straight, but curved lines for propellers with significant sweep may also be used. The only constraint is that the azimuthal positions and radial discretization of the sampling lines must be the same as those of the source term volume mentioned above.

Each node of the sampling lines is assumed to represent a blade section, with a specific airfoil, a chord length $c(r)$ and a pitch angle $\beta(r)$. By interpolation in the CFD flow field, each node also has an axial and a tangential velocity $V_{x,CFD}(r,\theta)$ and $V_{t,CFD}(r,\theta)$. The velocities extracted from CFD include both the free flow component V_0 and the velocity component δV due to the source terms or to interaction effects. However, because the computation is in the absolute frame, the sampled tangential velocity $V_{t,CFD}(r,\theta)$ does not account for the component due to blade rotation, which must be included in the relative velocity computation (equation (2)).

$$V_{x,rel}(r,\theta) = V_{0,x} + \delta V_x(r,\theta) = V_{x,CFD}(r,\theta) \tag{1}$$

$$V_{t,rel}(r,\theta) = \Omega r - \left(V_{0,t}(\theta) + \delta V_t(r,\theta)\right) = \Omega r - V_{t,CFD}(r,\theta) \tag{2}$$

$$V_{rel}(r,\theta) = \sqrt{V_{x,rel}(r,\theta)^2 + V_{t,rel}(r,\theta)^2} \tag{3}$$

The relative velocities and pitch angle give the local flow angle with the blade section $\phi(r,\theta)$, and the effective angle of attack $\alpha(r,\theta)$ (equations (4) and (5)). The calculation of the angles is summarized in Figure 10a for a case without incidence.

$$\phi(r,\theta) = \arctan\left(\frac{V_{x,rel}(r,\theta)}{V_{t,rel}(r,\theta)}\right) \tag{4}$$

$$\alpha(r,\theta) = \beta(r) - \phi(r,\theta) \tag{5}$$

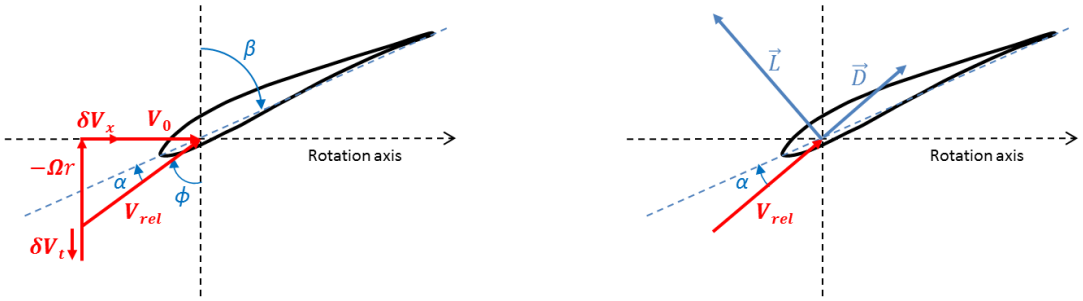

(a) Computation of the angle of attack **(b) Computation of sectional loads**

Fig. 10 Blade Element Theory applied to a propeller section for axial flow.

The lift and drag coefficients $C_l(\alpha(r,\theta), M(r,\theta), R_e(r,\theta))$ and $C_d(\alpha(r,\theta), M(r,\theta), R_e(r,\theta))$ are interpolated at each sampling line node from a set of 2D airfoil polars, as in the lifting-line approach. The lift and drag forces are then computed from equations (6) and (7). It is important to note that because the model assumes a 2D flow on the blade, no radial force component is included (Figure 10b). The radial velocity component is also not taken into account in the computation of the relative velocity $V_{rel}(r,\theta)$ (equation (3)).

$$\frac{dL}{dr}(r,\theta) = \frac{1}{2}\rho c(r) V_{rel}(r,\theta)^2 C_l(r,\theta) \tag{6}$$

$$\frac{dD}{dr}(r,\theta) = \frac{1}{2}\rho c(r) V_{rel}(r,\theta)^2 C_d(r,\theta) \tag{7}$$

$\boldsymbol{L}(r,\theta)$ and $\boldsymbol{D}(r,\theta)$ are summed and projected from the local blade section frame into the CFD computation frame to obtain the loads at each blade radius and azimuth $\boldsymbol{f_{BET}}(r,\theta) = (f_{BET,x}(r,\theta), f_{BET,y}(r,\theta), f_{BET,z}(r,\theta))$ in N.m^{-1}. N_j blade loads have been computed instead of N_b, so in order to distribute the right amount of force into the computation, $\boldsymbol{f_{BET}}(r,\theta)$ needs to be scaled:

$$\boldsymbol{f_s}(r,\theta) = \frac{N_b}{N_j}\boldsymbol{f_{BET}}(r,\theta) \tag{8}$$

3. Source Terms Computation and Distribution

Once the loads are computed, the sampling lines are stacked into a surface (referred to as "sampling surface"), and the loads moved to the cell centers. They are then transformed into force densities and distributed axially into the source term volume. Each cell of the sampling surface is associated to a volume $V_e(r)$ of the source term volume, which is located at the same radial and azimuthal position (Figure 11). This volume is composed of N_k cells in the axial direction. To obtain a uniform distribution of the source terms over the auxiliary mesh in the axial direction, the force

density in each cell must be:

$$\boldsymbol{f_d}(r,\theta) = \frac{dr(r)}{V_e(r)}\boldsymbol{f_s}(r,\theta) \tag{9}$$

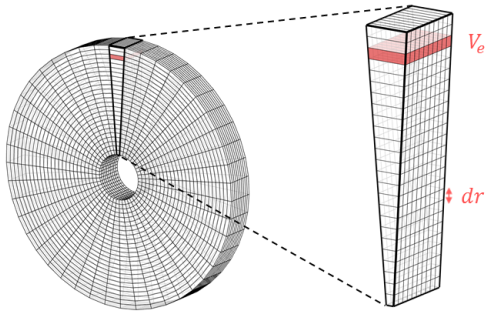

Fig. 11 Definition of the cell extrusion volume V_e.

As discussed previously, a weight function $w_e(r,x)$ can also be applied to the sources to change the distribution in the axial direction as long as it is divided by a normalization factor $F_n(r)$. The final form of the distributed source terms is then:

$$\boldsymbol{f}(r,\theta,x) = \frac{w_e(x)}{F_n(r)}\boldsymbol{f_d}(r,\theta) \quad \text{where} \quad F_n(r) = \frac{\sum_k w_e^k V^k}{\sum_k V^k} \tag{10}$$

The source term field $\boldsymbol{f}(r,\theta,x)$ is then injected into the CFD computation by interpolation from the source term volume to the computational mesh and is accounted for in the right-hand-side of the RANS equations at the next CFD iteration (Figure 9d).

4. Resolution Process

A CFD simulation is started on the computational mesh. The source terms are recomputed as described above every 20 RANS iterations so the flow can stabilize in the area of the propeller before the sources are updated again. This is repeated until the computation is converged, which takes about 5000 iterations.

IV. Study and Analysis of the RANS/BET Body Force Model

For the RANS/BET method, the previous section shows that several choices have to be made regarding the construction of the loads and their distribution: (i) the shape of the volume where the source terms are applied, (ii) the relative position within this volume of the sampling lines where the local flow parameters are extracted and (iii) the axial distribution of the forces. In this section, several options for these parameters are discussed and tested, and their influence on the resulting loads and flow fields are investigated. All the computations are done for the propeller presented in section II, for a zero incidence angle.

A. Influence of the Source Term Volume

As mentioned in section III.C.1, the source term volume can be chosen to have any shape as long as it is coherent with the sampling lines. In this section, three different shapes are compared, which are represented in Figure 12. The options considered are the volume swept by the blades in a blade-resolved simulation (labeled 'fitted box'), a cylinder that has the same length as the volume swept by the blades (labeled 'bounding box') and another cylinder that has a length of $1.5 * c_{max}$ (labeled 'extended box').

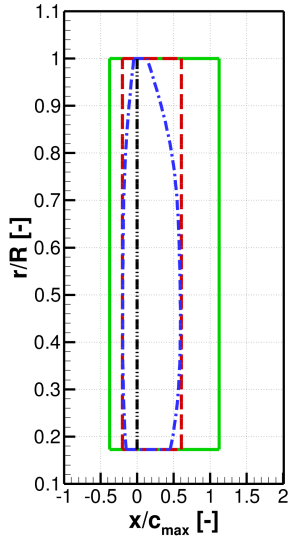

Fitted box (----), Bounding box (— —), Extended box (——), Sampling line (-·-·-)

Fig. 12 Sections of source term volumes.

For all cases, the sampling lines are placed at x=0, corresponding to the stacking line of the propeller's blade sections, which is at 25% of the chord for all spanwise sections. The volumes are placed so that their upstream boundaries are 25% of the volumes' axial length upstream of the sampling lines, as in Figure 12. The axial distribution of the source terms replicates the setup proposed by Ortun and relies on the calibrated Weibull density function used in Ref. [15], which mainly distributes the sources at the upstream part of the volume, as shown in Figure 14. The reasons behind this setup will be explained by the results in the rest of section IV.

A RANS/BET simulation was run for each volume shape. The radial distributions of the axial and tangential loads evaluated by the BET are plotted in Figures 13a and 13b. A flow field analysis downstream of the propeller is also made. Figures 13c and 13d show the radial profiles of the axial and tangential velocities half a propeller radius downstream of the sampling lines.

In all these figures, the curves for the different volumes are all superimposed. An analysis of the flow field further downstream, not shown here, leads to the same observation. The number of cells the source term volume has in the axial direction was also found to have no impact on the results. It can therefore be concluded that the shape of the source term

volume has no impact on the results of the model. It should be noted here that: (i) this is an important finding as this question is rarely directly addressed in literature on similar methods, (ii) and that this conclusion is in fact related to the choice of how the axial distribution is made, as will be demonstrated in the next section. In the rest of the paper the source terms are always distributed in a volume shaped as the extended box. This is done to relax the constraint on cell-size for the interpolation of the source terms into the computational mesh.

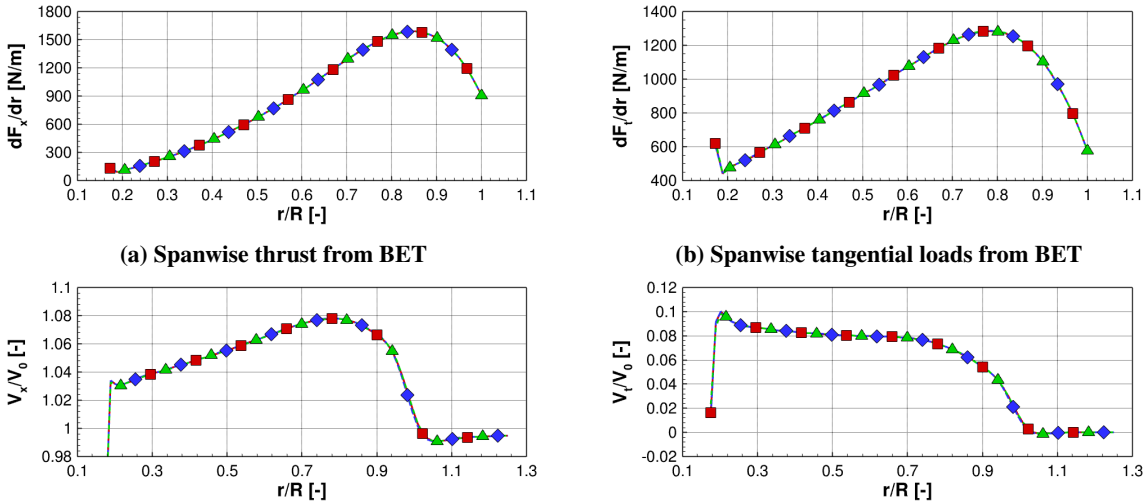

(a) Spanwise thrust from BET **(b) Spanwise tangential loads from BET**

(c) Axial velocity field **(d) Tangential velocity field**

Fitted box (- - ◆ - -), Bounding box (—■—), Extended box (– ▲ –)

Fig. 13 Computation results for three shapes of source term volumes.

B. Influence of Source Term Axial Distribution and Velocity Sampling

A Gaussian projection kernel is commonly employed in the literature to directly distribute source terms into the CFD computational mesh, without resorting to interpolations [10, 13]. However other distribution functions can be used. Actually, thin airfoils operating at subsonic conditions have their aerodynamic center close to the quarter chord. This property can be reproduced in a RANS/BET body force simulation by using a weight density to unevenly distribute the source terms in the axial direction. For example, a Weibull density function can be used, as done by Ortun [15].

To quantify the influence of the source term distribution on the RANS/BET results, we consider here three axial distribution densities: uniform, Gaussian and Weibull (Figure 14). For each one, three computations are made in which the velocity sampling lines are placed so that 25%, 50% and 75% of the source terms are distributed upstream of them.

Figures 15a and 15b show the radial distribution of axial and tangential loads for each computation. Figures 15c and 15d show the axial and tangential velocities half a propeller radius downstream of the rotation center. For a given percentage of the sources distributed upstream of the sampling lines, all the tested distribution functions lead to identical blade loads and flow fields. This result clearly shows that the shape of the axial distribution function has no direct impact

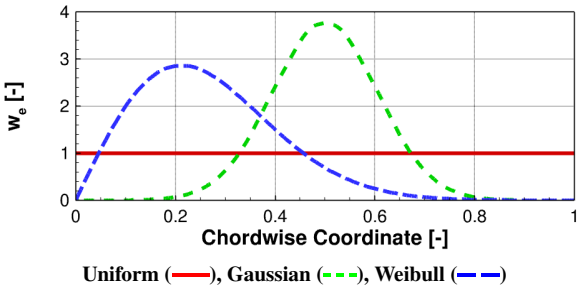

Fig. 14 Density functions used for axial distribution of source terms.

on the results, which can be interpreted physically. Since no radial forces are applied in the body force volume, a fluid particle travels through the volume at approximately the same radius. The flow being axisymmetric, the acceleration seen by the fluid particle throughout its movement in the body force volume is a constant modulated by the normalized distribution function. As such, the integral of the acceleration over a given streamline is the same regardless of the distribution function. The validity of this result when the propeller operates at incidence will be evaluated in section VI.C.

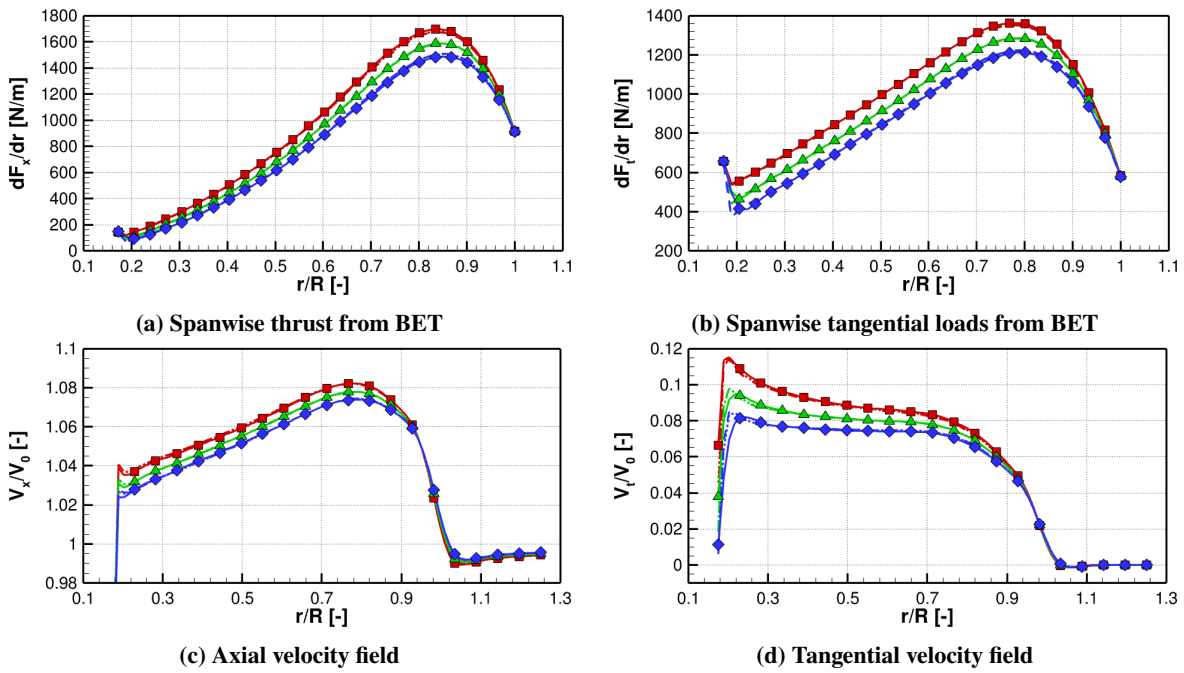

Fig. 15 Computation results for different source terms distributions.

The only parameter that has an effect on the results is the quantity of source terms that is distributed upstream of the sampling lines. This parameter is critical because if more sources are placed upstream of the sampling lines,

the velocities used for the BET will be higher, resulting in lower angles of attack and lower blade section loadings. Conversely, if less source terms are placed upstream of the sampling lines, the induced velocities will be low and the efforts higher. This system is stable but its convergence point still depends on the location used to evaluate the velocities used in BET, as shown in Figure 15.

C. Comparison to Blade Element Momentum Theory

The previous sections have shown that the RANS/BET method's key parameter is the quantity of source terms that is distributed upstream of the velocity sampling lines. To correctly choose this parameter, velocities in the wake of the propeller are compared in this section with classical BEMT results, which are recalled hereafter and summarized in Figure 16. Froude's momentum theory for actuator disks models the propeller as a pressure jump that guarantees axial velocity continuity. It states that, under a few assumptions, the induced axial velocity in the wake far downstream is twice that in the disk plane [41, 42]. Glauert also shows in the blade element momentum theory that the tangential velocity induced by an actuator disk is discontinuous, its value immediately downstream of the rotor plane being twice the one in the actuator disk plane [1]. When the wake contraction is limited, as it is the case for a lightly loaded propeller such as HAD-1, this tangential velocity is constant in the wake by Kelvin's theorem.

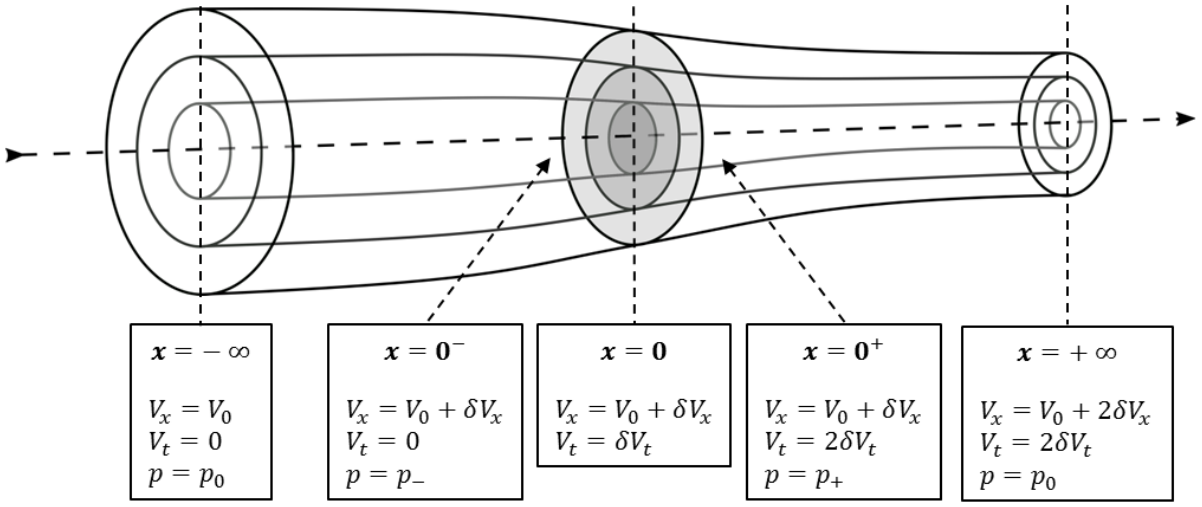

Fig. 16 Summary of fundamental BEMT results.

Only the flow field induced by the body force is relevant for comparison with BEMT. It is obtained by subtracting the velocity field of a RANS computation (accounting for the spinner and hub but without source terms) from a RANS/BET computation (accounting for the spinner, the hub, and source terms). This is done to isolate the contribution of the propeller to the flow field from the distortion of the flow by the spinner and the hub. In the RANS/BET computation, 50% of the source terms are distributed upstream the velocity sampling lines and the rest downstream, using a Gaussian axial distribution.

Figure 17 shows longitudinal slices of axial velocity, tangential velocity, and pressure fields induced by the body forces. The limits of the body force domain is represented with white lines. The first slice clearly shows the continuity of axial velocity through the body force region, whereas the other two show tangential velocity and pressure jumps, as in the BEMT theory. A more in depth analysis, not shown here, revealed that these jumps are very sudden when using axial distribution functions that smear the source terms over a small region (Gaussian or Weibull distributions), and much smoother when using a uniform distribution. However, the axial velocity flow fields were found to be nearly identical, even within the body force volume, regardless of the distribution function. In all cases, the flow fields were found to be identical outside the body force volume, as seen in the previous section.

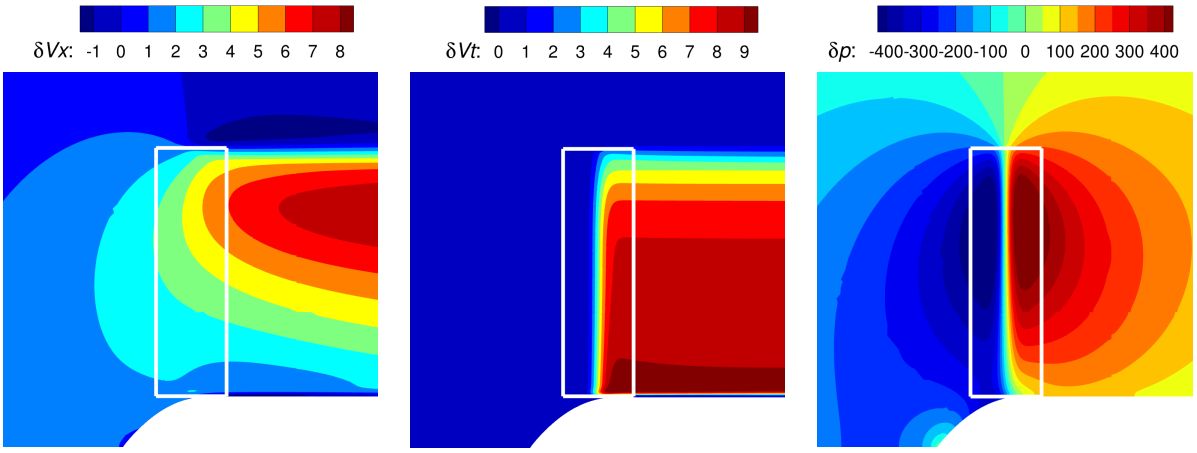

(a) Axial induced velocity field **(b) Tangential induced velocity field** **(c) Induced pressure field**

Fig. 17 Longitudinal slices of fields induced by the body forces.

Figure 18 shows the radial variation of the induced axial and tangential velocities for RANS/BET and BEMT computations at different axial locations (labeled 'BF'), where $X = 0$ is the propeller plane (ie., the velocity sampling plane in RANS/BET). The theoretical value of the induced flow far downstream is also plotted (labeled 'Froude and Glauert Theory'), which is obtained by multiplying the RANS/BET velocity fields from the propeller plane by 2, as it is the case in the BEMT.

For the induced axial velocity, the radial distributions tend progressively toward the theoretical value predicted by Froude's theory. For the induced tangential velocity, Glauert's theoretical value is reached rapidly behind the propeller. The velocity profile then stays constant downstream because the wake contraction is negligible. Both these observations would evidently not be the same if more or less than 50% of the source terms were distributed upstream the propeller. Indeed if less sources are distributed upstream, the induced velocities are lower in the rotor plane and much higher downstream, leading to a velocity ratio much larger than 2. It is the opposite if more than 50% of sources are distributed upstream.

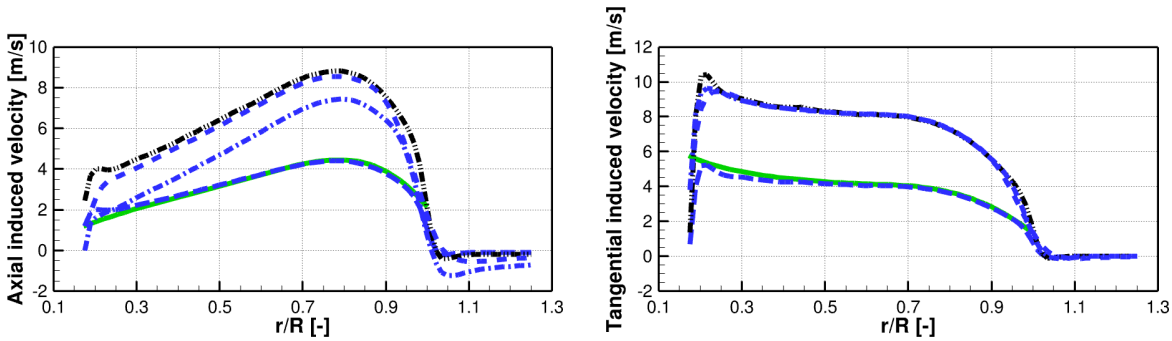

(a) Spanwise axial velocity profiles **(b) Spanwise tangential velocity profiles**

BF $X = 0$ (——), **BF** $X = 0.5 * R_{tip}$ (-·-·-), **BF** $X = 3.5 * R_{tip}$ (- - -), **Froude and Glauert Theory** (-··-··-), **BEMT** $X = 0$ (——)

Fig. 18 RANS/BET and BEMT induced velocity profiles comparison.

Figure 18 also shows that the induced velocities in the rotor plane computed by BEMT are almost identical to those computed by RANS/BET, which further shows that the source terms are correctly distributed in the RANS/BET computation and that the velocities are correctly sampled.

These results therefore show that in order to verify the founding results of the BEMT, the source terms should be equally distributed upstream and downstream of the sampling lines. This is interesting because it is what some authors do without detailed justification. Ortun [15] and Reboul et al. [16] use a calibrated Weibull axial distribution and place the source term volume 25% of its length in front of the sampling plane. By integrating the Weibull function in the axial direction, it can be shown that this setup corresponds to a distribution of 50% of the source terms upstream the sampling lines. Sørensen et al. [10] distribute the source terms using a Gaussian density centered on the sampling lines, which also corresponds to a distribution of 50% of the source terms upstream of the sampling lines. In the rest of the paper, half the source terms are distributed upstream of the sampling plane, and half downstream.

V. Tip-Loss Correction

Different source term distribution methods have been evaluated and an optimal setup has been found. The RANS/BET model needs to be further refined by adding a tip-loss correction to better match the RANS blade-resolved results. The two following sections explain why a tip-loss correction is necessary, and assess four tip-loss corrections, including two from the literature.

A. RANS/BET Computation with Prescribed Loads

In this section, the radial loads are prescribed using the results from the RANS blade-resolved approach instead of being computed using BET. The objective is to evaluate how accurately the body force computation can restitute

the velocity fields from the correct radial loads. Figure 19 shows the azimuthal average of the velocity fields half a radius behind the propeller computed by RANS with a blade-resolved approach, and the velocity fields computed by the RANS/BET with prescribed loads. The trends of the blade-resolved computation are very well restituted by RANS/BET for both the axial and tangential velocity fields.

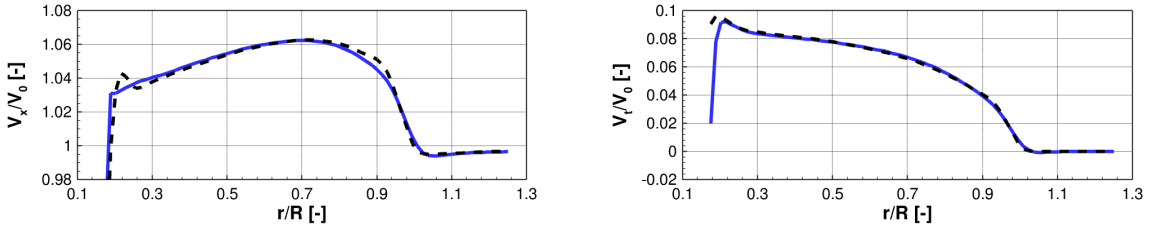

(a) Azimuthal average of axial velocity field **(b) Azimuthal average of tangential velocity field**

RANS blade-resolved (- - -), RANS/BET with prescribed loads (——)

Fig. 19 Velocities from RANS/BET computation with prescribed forces.

At the end of the RANS/BET computation with prescribed loads, the disk loads are recomputed by BET from the velocity fields of the solution. The objective is now to evaluate if the right loads can be computed from BET if the velocity fields are correct. Figure 20 shows the radial distribution of the axial and tangential loads that are prescribed in the body force computation and the loads that are recomputed by BET from the velocity fields. The results show that the loads are overestimated by the BET computation by up to 40% near the tip of the blades.

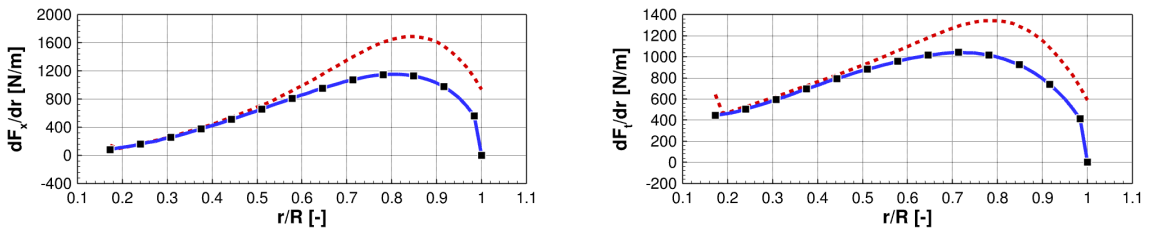

(a) Spanwise thrust **(b) Spanwise tangential loads**

RANS blade-resolved (■), Loads prescribed in body force computation (——), Loads recomputed by BET (- - -)

Fig. 20 Blade loads from RANS/BET computation with prescribed forces.

This section thus shows that the correct velocity fields are restituted by the body force computation if the correct radial loads are prescribed. However, BET greatly overestimates the loads at the blade tip from the correct velocity fields. This confirms the well-known result that the sampled velocities or the BET loads need to be corrected in order for the RANS/BET approach to be accurate [1, 17]. This correction corresponds to the tip-loss correction, which is investigated in the following section.

B. Assessment of Tip-Loss Corrections

As explained previously, the RANS/BET method solves a time-averaged field over a full propeller revolution. As a result, the flow field does not include any local perturbation due to the physical presence of distinct blades, such as tip vortices. This leads to lower induced velocities in the sampling plane and thus overestimated loads at the blade tips. This is not the case for lifting-line computations, which solve the distinct blades and account for the tip vortices using a free wake model. Figure 21 represents a slice of the velocity fields in the propeller plane for both methods and clearly shows the absence of tip vortices in the RANS/BET computation. This limitation is inherent to the method and corrections must be applied to increase fidelity. Two types of corrections are commonly applied in the literature. The most physically coherent method is to correct the sampled velocities to artificially account for local perturbations, especially near the blade tips. Another method is to directly use the sampled velocities to compute the loads with BET and apply a radial correction factor on the loads afterward.

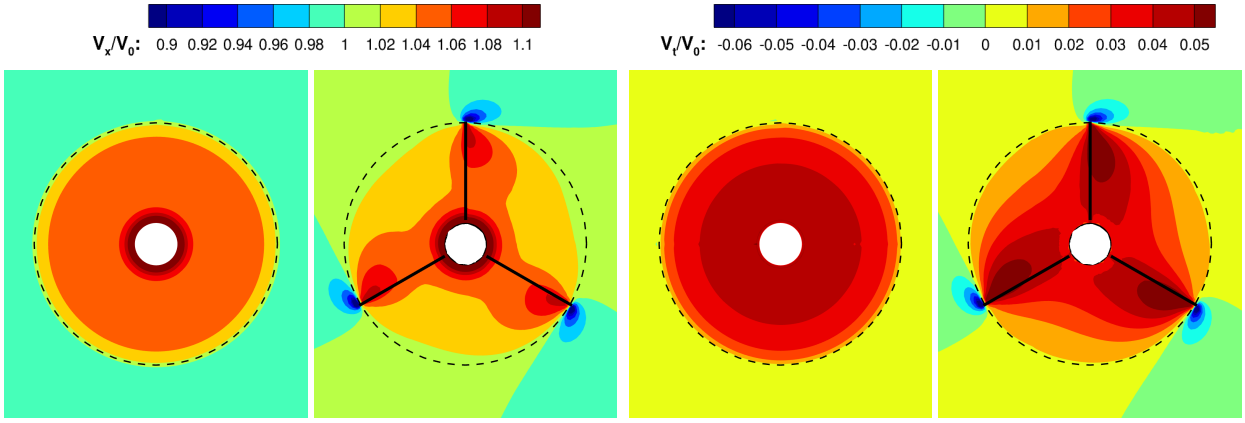

(a) V_x/V_0 **- RANS/BET** **(b)** V_x/V_0 **- Lifting-line** **(c)** V_t/V_0 **- RANS/BET** **(d)** V_t/V_0 **- Lifting-line**

Fig. 21 Velocity fields in rotor plane from RANS/BET and lifting-line computations.

Four tip-loss corrections are tested and compared in the following. This procedure is similar to the one conducted by Zhong et al. [14] for wind turbine applications.

1) **Glauert correction.** It corrects the sampled velocities using a factor derived by Glauert for the BEMT [1]. It is implemented using an iterative procedure described by Shen et al. [23].
2) **Glauert + Shen et al. correction.** The Glauert correction does not account for 3D flow and thus does not predict a zero load at the very blade tip due to pressure equalization between the pressure and suction sides. To account for this, Shen et al. [23] suggest to correct the blade loads at the very tip using a factor F_{Shen}, in addition to using the Glauert correction. F_{Shen} has the same shape than the Glauert factor but with an additional coefficient g that depends on the number of blades and the tip speed ratio. The correction factor is implemented by changing equations (6) and (7) to:

$$\frac{dL}{dr} = \frac{1}{2}\rho c V_{rel}^2 C_l * F_{Shen} \tag{11}$$

$$\frac{dD}{dr} = \frac{1}{2}\rho c V_{rel}^2 C_d * F_{Shen} \tag{12}$$

$$\text{with } F_{Shen} = \frac{2}{\pi}\cos^{-1}\left[\exp\left(-g\frac{N_b(R-r)}{2r\sin\phi}\right)\right] \tag{13}$$

$$\text{and } g = exp(-0.125(N_b\Omega R/V_0 - 21)) + 0.1 \tag{14}$$

3) **Glauert + calibrated loads correction.** The authors propose here a tip-loss correction that uses the Glauert correction of the sampled velocities and lowers the loads using a correction factor F_C. The latter is designed to reduce the difference in spanwise thrust between the RANS/BET simulation with Glauert correction, and the blade-resolved simulation. The ratio $(dF_x/dr)_{BladeResolved}/(dF_x/dr)_{RANS/BET}$ is modeled by analogy with Shen et al.'s factor by equation (15) where g_1, g_2 and d_r are calibration coefficients chosen to best fit the ratio over the blade span. F_C is then implemented as for the previous correction in equations (11) and (12) by replacing F_{Shen} with F_C defined by:

$$F_C = \frac{2}{\pi}\cos^{-1}\left[\exp\left(-g_1\frac{N_b(R-r)}{2r\sin\phi}\right)\right] * \frac{2}{\pi}\cos^{-1}\left[\exp\left(-g_2\frac{N_b(d_r-r)}{2r\sin\phi}\right)\right] \tag{15}$$

4) **Calibrated loads correction.** It is the same as the previous correction, but without the correction of sampled velocities. The correction F_C is computed as the ratio of the spanwise thrust from the blade-resolved simulation and from the RANS/BET simulation without any tip correction. The constants g_1, g_2 and d_r are thus different from the previous correction.

The simulations using the previously detailed corrections are compared to a RANS/BET computation without a tip-loss correction and to a blade-resolved CFD-RANS computation. The propeller thrust, power and efficiency computed by each approach are given in Table 5. The radial distribution of thrust and tangential loads are presented in Figure 22.

Table 5 Integrated loads for each tip-loss correction

Modeling method	Thrust [N]	Power [kW]	Efficiency [-]
RANS blade-resolved	1390	164.4	0.863
RANS/BET - no correction	1748 (+25.7%)	199.1 (+21.1%)	0.896 (+3.3pts)
RANS/BET - Glauert	1574 (+13.3%)	184.3 (+12.1%)	0.872 (+0.9pts)
RANS/BET - Glauert + Shen	1514 (+9.0%)	176.8 (+7.5%)	0.874 (+1.1pts)
RANS/BET - Glauert + loads calibration	1426 (+2.6%)	167.3 (+1.8%)	0.870 (+0.7pts)
RANS/BET - loads calibration only	1438 (+3.5%)	162.9 (-0.9%)	0.901 (+3.8pts)

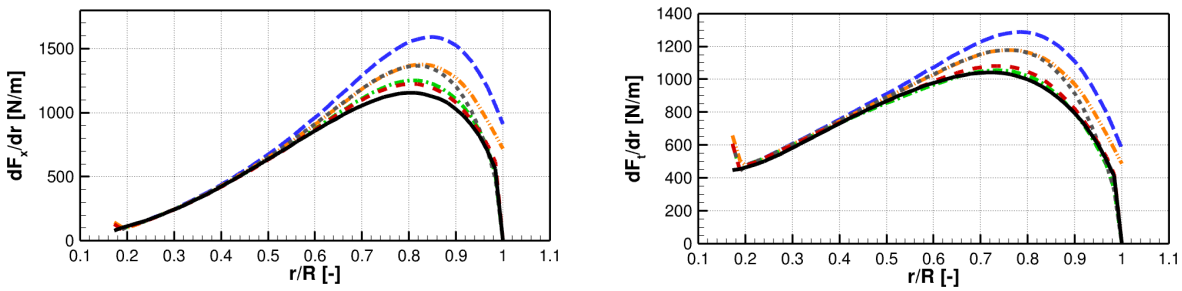

(a) Spanwise thrust **(b) Spanwise tangential loads**

RANS/BET - no correction (— —), RANS/BET - Glauert (-··-), RANS/BET - Glauert + Shen (·····),
RANS/BET - Glauert + loads calibration (- - -), RANS/BET - loads calibration (-·-·-), RANS blade-resolved (——)

Fig. 22 Radial distribution of loads for each tip-loss correction.

The Glauert correction leads to a good prediction of the efficiency but does not reduce the thrust and power sufficiently. The same observation is made when the Shen et al. correction is added, despite a more accurate prediction at the very tip of the blade. The Glauert + calibrated loads correction gives a good prediction of the propeller thrust, power and efficiency. The spanwise loading is also very close to the blade-resolved results despite a slight overestimation that persists near the tip. The calibrated loads correction alone is rather accurate on spanwise loads but poorly predicts the propeller efficiency. Because this method does not correct the sampled velocities, the lift and drag coefficients interpolated in the 2D profile characteristics are necessarily not the correct ones. The correction of the thrust with F_C brings it down to the right value, but the same factor has no reason to be suited for the torque as well. This observation highlights that, contrary to sampled velocity corrections, the loads correction has an arguable physical significance when applied elsewhere than at the very tip of the blade to model 3D effects. For example, the computation of an effective angle of attack directly from the sampled flow may hit a detached point in the 2D airfoil characteristics, whereas it would have hit an attached point if the sampled velocity had been corrected first, thus leading to a drastically different lift to drag ratio, even if the loads are corrected by F_C afterwards. This observation is also true for the Glauert + loads calibration correction, even if the correction is satisfying in this case. In order to replicate the flow physics as well as possible, it would be best to use a calibrated correction of sampled velocities and a Shen et al. correction of the loads to account for 3D effects at the very tip of the blades. However, the correction of the sampled velocities changes simultaneously α and V_{rel}, which modifies C_l and C_d by interpolation, thus finally modifying the loads. This deep coupling makes it difficult to calibrate a sampled velocities correction. As a result, the Glauert + loads calibration correction was used in the rest of the paper and its validity for other propeller operating points with different blade loadings will be investigated in section VI.B.

The wake velocity profiles one radius behind the propeller for each computation are represented in Figure 23. They show a direct correlation between loading overshoot and wake velocity overshoot. It is important to note that the coefficients used for the calibrated tip-loss are specific to a given propeller. In theory, any propeller geometry

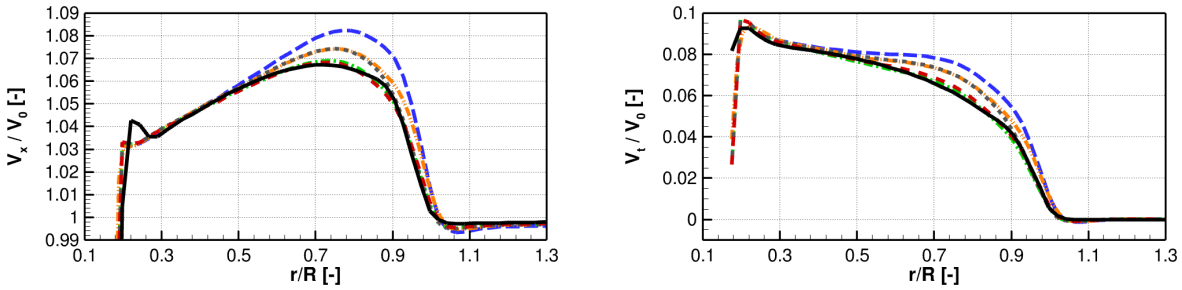

(a) Spanwise axial velocity profiles

(b) Spanwise tangential velocity profiles

RANS/BET - no correction (— —), RANS/BET - Glauert (-·-·-), RANS/BET - Glauert + Shen (·····),
RANS/BET - Glauert + loads calibration (- - -), RANS/BET - loads calibration (-·-·-), RANS blade-resolved (——)

Fig. 23 Wake velocity profiles for each tip-loss correction.

modification changes the circulation distribution over the blade span and modifies the tip vortex, which in turn should require a new specific tip-loss correction. In practice, a small change in twist or chord distribution that does not modify the tip vortex structure significantly may not require a new calibration, but this has not been tested in the current work. As a result, this type of correction is not the best suited for a wide parametric exploration for propeller design. It can however be very effective to evaluate the performance of a given propeller on the aircraft on which it is installed when conducting installed simulation.

VI. Assessment of the Final RANS/BET model

In this section the final RANS/BET model, which distributes the source terms as recommended in section IV and uses the tip loss correction retained from section V.B, is thoroughly compared to the RANS blade-resolved and lifting-line methods. This comparison is first done on the cruise operating point, then on several blade pitch angles, and finally in non axial flow by adding an incidence angle. This is done to evaluate the accuracy of the RANS/BET model in typical applications, and on other operating points than the one used for the tip-loss calibration.

A. Comparison at Cruise Operating Point

The free flow conditions studied in this sections are still the ones from Table 2. The integrated loads obtained for each modeling approach are shown in Table 6. The propeller thrust and power are slightly overestimated by the lifting-line and RANS/BET body force approaches compared to RANS blade-resolved but the efficiency is quite accurate. The body force prediction is especially close to the CFD results thanks to the calibrated tip correction.

The spanwise distribution of axial and tangential blade loads are shown in Figure 24. On the first half of the blade span, the lifting-line and body force methods predict the blade-resolved loads very accurately. Both methods over predict the maximum spanwise thrust by about 6% close to the tip. The maximum tangential load is also overestimated, by 8% for the lifting-line method and by 5% for the body force method.

Table 6 Integrated loads for each approach

Modeling method	Thrust [N]	Power [kW]	Efficiency
RANS Blade-Resolved	1390	164.4	0.863
Lifting-Line	1463 (+5.3%)	174.0 (+5.8%)	0.858 (-0.5pts)
RANS/BET	1426 (+2.6%)	167.3 (+1.8%)	0.870 (+0.7pts)

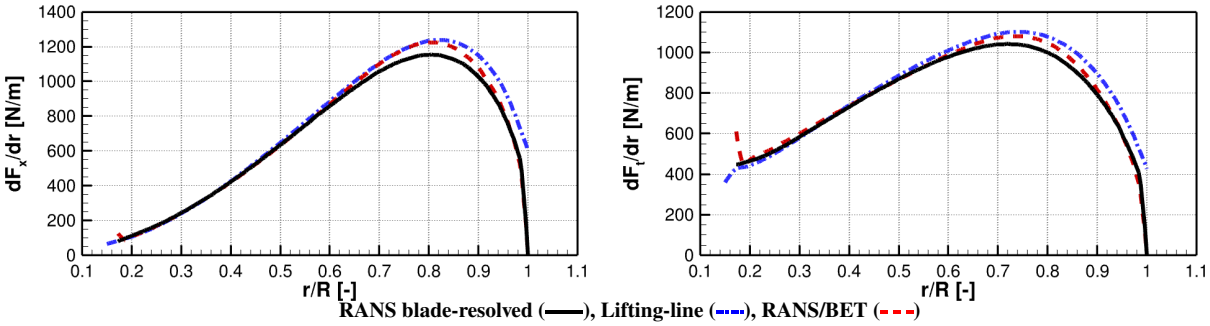

Fig. 24 Axial and tangential loads computed by the three methods.

The velocity fields downstream of the propeller are also studied. Figure 25 shows the spanwise variation of the azimuthal average of velocity profiles one radius downstream of the propeller. Both mid-fidelity methods reproduce the CFD trends accurately. The lifting-line approach slightly overestimates the axial velocity and underestimates the tangential velocity compared to CFD. The body force velocity profiles fit the CFD profiles remarkably well.

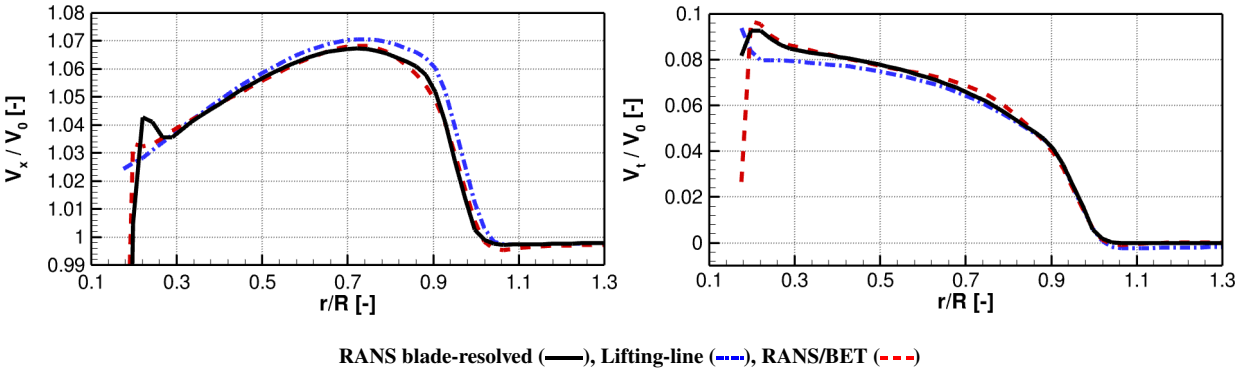

Fig. 25 Azimuthal average of axial and tangential velocity profiles one radius behind the propeller.

B. Propeller Pitch Variation

Propeller performance is also evaluated for different blade pitch angles for the RANS blade-resolved, lifting-line and RANS/BET body force approaches. The propeller thrust and efficiency as function of blade pitch and thrust are shown in Figure 26. The lifting-line and body force approaches follow the RANS blade-resolved efficiency trends accurately, the differences going from 0 to 0.5 efficiency point. Figure 26a shows that for a given pitch angle the lifting line approach overestimates the thrust much more than the body force method, but by also overestimating the power it still gives a more accurate efficiency-thrust curve than the RANS/BET method.

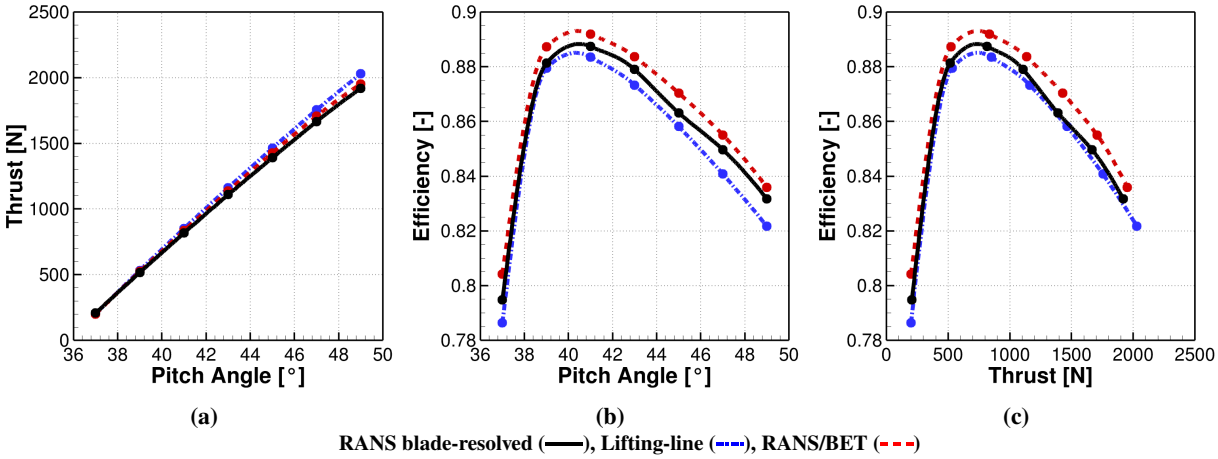

Fig. 26 Propeller characteristics.

C. Propeller in incidence

In this section, the performance of the final RANS/BET body force model is investigated in non-axial flow conditions. The propeller is taken at a 45 degree pitch angle for incidence angles Θ of 3, 6, and 9 degrees. The downward moving blade (advancing side) sees a greater velocity than the upward moving one (retreating side), leading to a non-axisymmetric disk load (Figure 27). The blade load variation throughout a propeller revolution also leads to the appearance of a non-zero in-plane (1P) force when adding the contribution of each blade. These loads are limiting for aircraft structures and must be well predicted during the design phase. In this paper the 1P loads are studied as a modulus and a phase angle (defined by the conventions of Figure 27). The modulus corresponds to the norm of the in-plane force, and the phase corresponds to the angle between the 1P force vector and the upward axis.

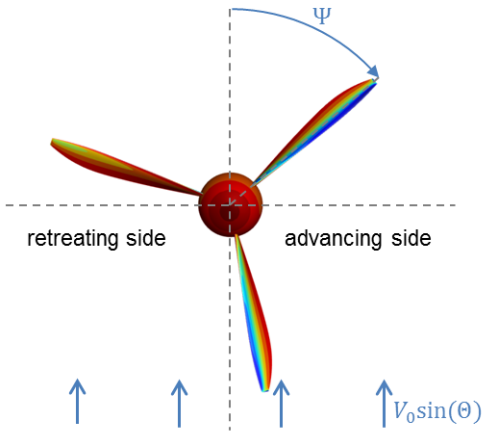

Fig. 27 HAD-1 propeller under incidence colored by pressure.

To study these operating points, the blade resolved reference results were obtained using URANS simulations on a 360° domain, as described in section III.A. The RANS/BET setup that is used for these computations is the same

one that was used in the previous section: source terms distributed in the extended box with a uniform axial density, velocities evaluated at 50% of the source terms distribution, and Glauert correction of the induced velocities and calibrated loads correction on the 45° pitch angle axial flow case. As mentioned in section IV.A, the shape of the source term volume could have an impact on disk load and flow field for non axial flow. A comparison was made with a source term volume four times less thick than the extended box, for an incidence angle of 9°. Both loads and flow fields were found to be identical with the extended box case. This shows that the independence of the RANS/BET results to source term volume can in practice be generalized to much broader cases than axial flows.

Figure 28 shows the propeller thrust, power, 1P load modulus and 1P phase angle averaged over a full propeller revolution for the studied incidence angles. The RANS/BET model fails to predict the decline of the thrust for low incidence angles but still predicts the thrust within 8% for all incidence angles, which is similar to the lifting-line prediction. For all incidence angles the error on power is constant at around 2% for the RANS/BET model and 6% for the lifting-line method. These errors are acceptable for the RANS/BET method as its prime purpose is to restitute a rather accurate wake and not to be exact on propeller performance. Furthermore, all the computations shown here are conducted at a 45° pitch angle. In practice, these methods are always trimmed to match a given thrust. The prediction of the 1P loads modulus and 1P phase is very accurate for the RANS/BET method. This shows that the RANS/BET method is capable of correctly modeling the induced velocities when the propeller is under low incidence. Under higher incidences or lower advance ratios, the blade-vortex interactions are stronger and the RANS/BET simulations are no longer expected to perform as well. The lifting-line model does not have this problem and is thus expected to predict the 1P loads relatively well. It is the case for the modulus, but the phase is offset by around 15°. This shows that additional corrections would be needed when using the lifting-line method for cases with incidence.

In the following, the results are studied more in depth for the 9° incidence angle. The conclusions are similar for the other angles. Figure 29 shows blade thrust and tangential loads as functions of the azimuth angle for the three modeling methods. These curves are compared in the frequency domain in Table 7. The Fast Fourier Transform (FFT) results are limited to the first two frequencies, the next ones having negligible amplitudes. The URANS blade-resolved and RANS/BET curves are in phase whereas the lifting-line results are offset by around 10°, which is coherent with the 1P phase results shown previously.

To correctly restitute the wake, the RANS/BET integrated blade loads must be in phase with those computed by the URANS blade-resolved method, but their spanwise distributions also need to be similar. Figures 30 and 31 show the spanwise variation of axial and tangential loads over the whole disk for the three studied methods. Overall, both the RANS/BET and lifting-line methods replicate the blade-resolved trends very well. The RANS/BET approach slightly overshoots the loads at the tip of the blades, especially at the more loaded azimuths, but the prediction on the lower part of the blade is very accurate on the whole disk. The model replicates the tangential loads with more fidelity than the axial loads. This could be an effect of using a load correction as a tip-loss correction instead of only using a fully

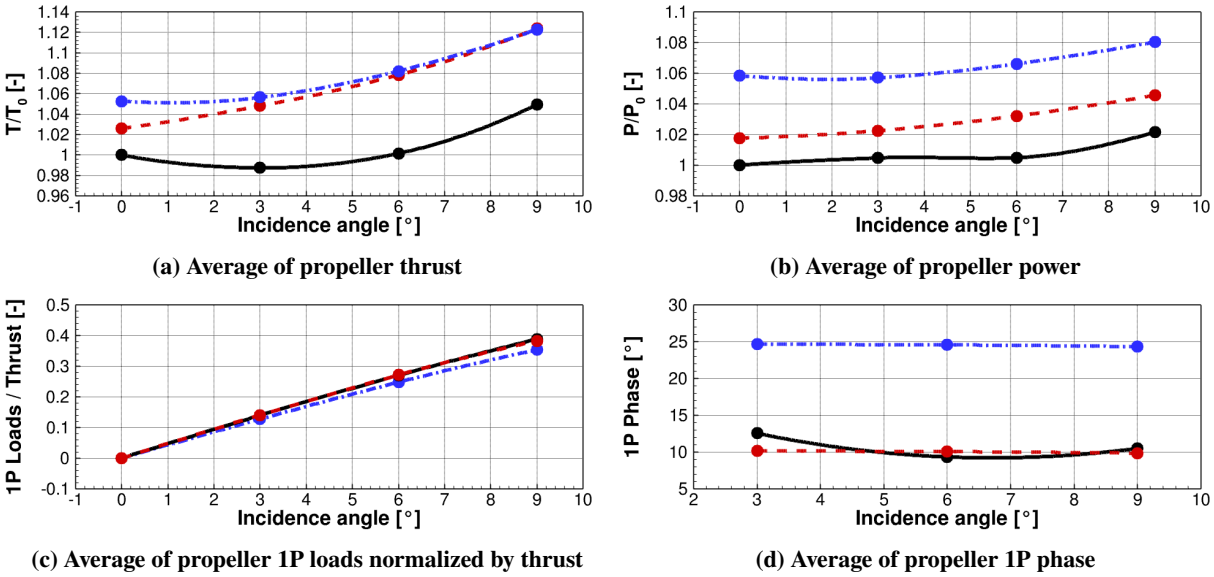

(a) Average of propeller thrust

(b) Average of propeller power

(c) Average of propeller 1P loads normalized by thrust

(d) Average of propeller 1P phase

URANS blade-resolved (——), Lifting-line (- - -), RANS/BET (– – –)

Fig. 28 Propeller performance averaged over a revolution for different incidence angles.

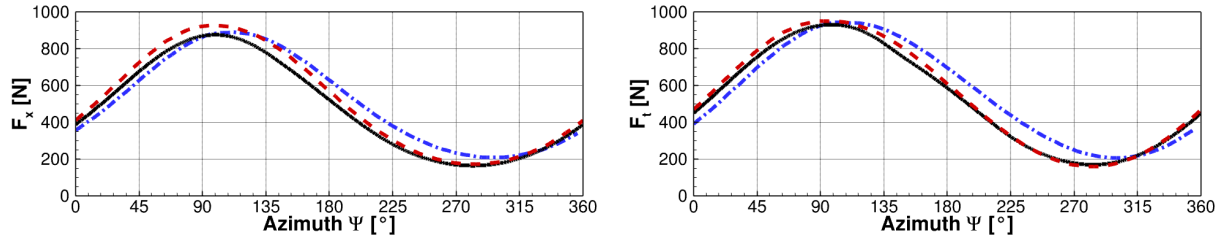

URANS blade-resolved (——), Lifting-line (- - -), RANS/BET (– – –)

Fig. 29 Blade axial and tangential loads over a revolution (9° incidence angle).

calibrated induced velocity correction. The lifting-line method seems to overshoot the tip load slightly less than the RANS/BET approach, but the load map is rotated compared to the URANS results, as noted previously.

Figure 32 shows the spanwise distribution of axial and tangential loads for the azimuth with the maximum efforts (top curve), the minimum efforts (bottom curve), and the average over all azimuths (middle curve). As shown previously, the azimuths of the max and min efforts are different for the three modeling methods. They are very close for the blade-resolved and RANS/BET methods, but are offset for the lifting-line method. The graph is actually quite similar to those found in section VI.A in axial flow. The curves almost overlap each other on the first part of the blade, and a slight overshoot persists when getting closer to the blade tip. For the RANS/BET method, this shows that the tip loss correction calibrated for an axial flow case in section V.B is still effective for a non-axial flow situation. However the overshoot grows as the blade becomes more loaded, indicating that the tip-loss correction could still be further refined. For the lifting-line method, the spanwise max and min loads are well predicted, but at the incorrect azimuths.

Table 7 Amplitude and phase coefficients of single blade loads obtained by Fourier analysis.

Component	Approach	Mode 0	Mode 1		Mode 2	
		Amplitude [N]	Amplitude [N]	Phase [°]	Amplitude [N]	Phase [°]
Axial	URANS	486	353	−101	33	168
	RANS/BET	521	380	−102	31	165
	Lifting-line	520	341	−113	32	149
Tangential	URANS	533	378	−100	20	−159
	RANS/BET	550	399	−100	12	−144
	Lifting-line	565	368	−114	21	−173

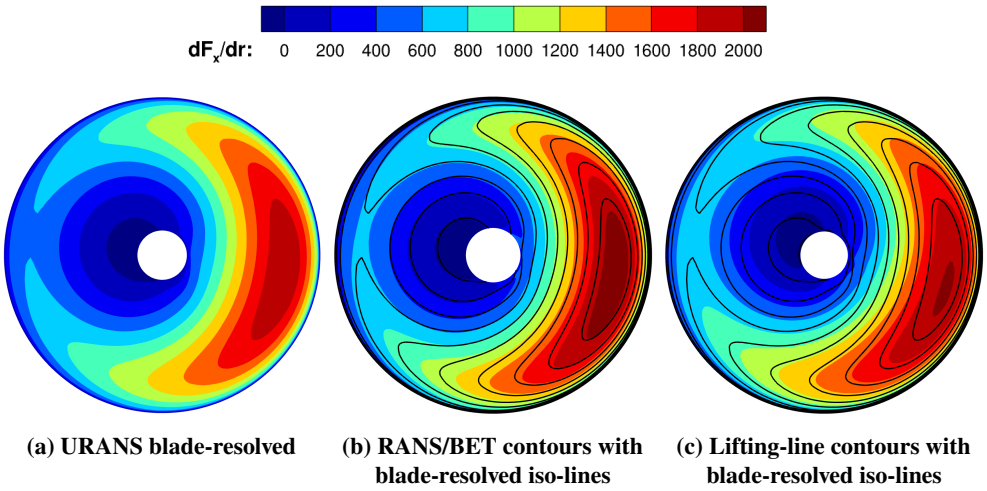

(a) URANS blade-resolved **(b) RANS/BET contours with blade-resolved iso-lines** **(c) Lifting-line contours with blade-resolved iso-lines**

Fig. 30 Distribution of blade axial loads over a revolution.

Furthermore, the loads overshoot at the tip seems to be constant regardless of the azimuth of the blade.

The main objective of the RANS/BET method is to correctly reproduce the time-averaged wake of an URANS blade-resolved computation. Figure 33 shows slices of the velocity field half a rotor radius downstream of the propeller, for the URANS blade-resolved and RANS/BET computations, for a 9° incidence angle. The velocity fields shown are those extracted from the CFD computation minus the free flow components. Figure 34 shows velocity profiles extracted from Figure 33 at azimuth angles of 0, 90, 180 and 270 degrees. The trends are overall very well predicted by the RANS/BET method for both axial and tangential flow. The maximum differences are very localized and within 10% of the blade-resolved induced velocities. As expected from the overshot efforts, the velocities are also generally slightly overestimated, especially in the axial direction. Trimming the propeller to the URANS blade-resolved thrust would fix this issue, but with a possible distortion in the radial direction. Figure 33c shows a vortex between the blade and the hub, which is shed at the azimuth where the blade is the most loaded. This corner separation can only be partly predicted by the RANS/BET method, as can be seen in Figures 34b, 34d and 34f. It is one of the limitations of this approach when

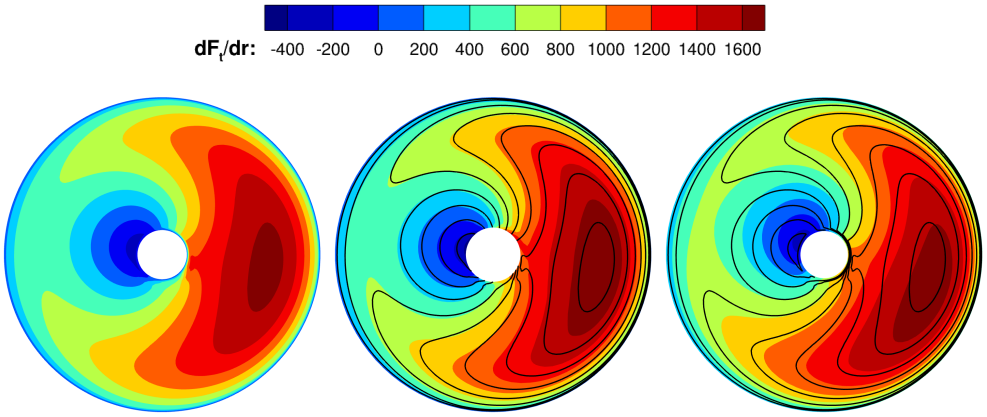

(a) URANS blade-resolved **(b) RANS/BET contours with blade-resolved iso-lines** **(c) Lifting-line contours with blade-resolved iso-lines**

Fig. 31 Distribution of blade tangential loads over a revolution.

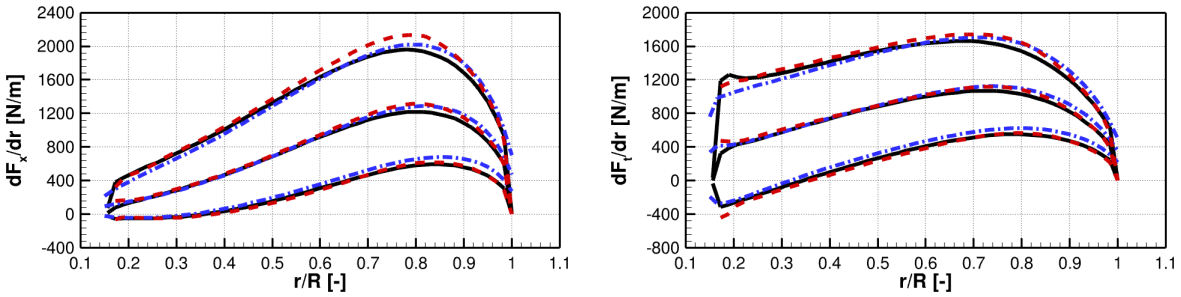

RANS blade-resolved (——), Lifting-line (- - -), RANS/BET (– – –)

Fig. 32 Max, mean and min axial and tangential spanwise blade loads over a revolution.

modeling flows with high incidence angles.

VII. Conclusions

This work presented a RANS/BET propeller modeling body force method. The approach is based on a full coupling between CFD which computes the flow field, and BET which computes the propeller loads using velocities sampled from the CFD computation. The loads are then accounted for in the CFD computations using source terms in the RANS equations. In this method, the source terms are distributed in a volume, which differs from classical actuator-disk-like approaches. This RANS/BET approach was tested on ONERA's HAD-1 three-bladed light propeller, and results were compared to lifting-line and RANS blade-resolved results.

Different source term distributions were thoroughly studied. The shape of the volume in which the source terms are distributed was found to have no impact on propeller loads or on velocity fields in the wake. This result was

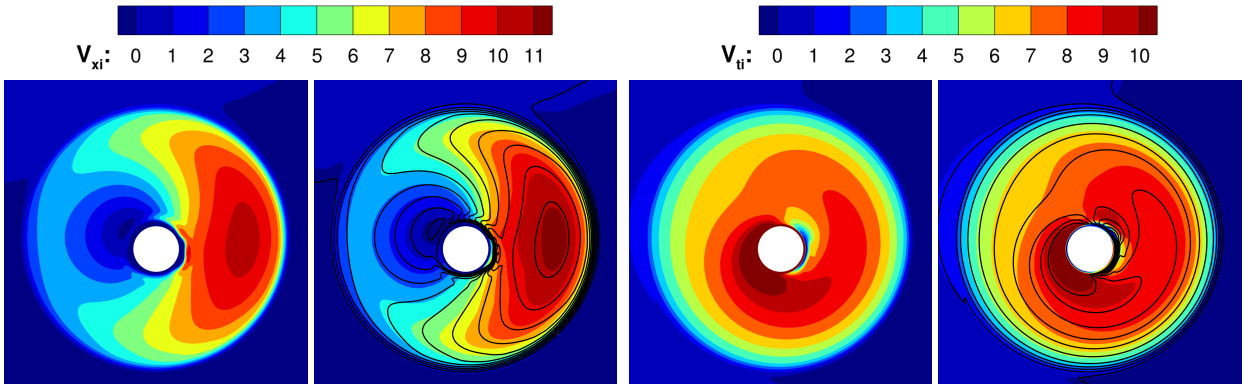

(a) V_{xi} **- URANS blade-resolved** **(b)** V_{xi} **- RANS/BET with blade-resolved iso-lines** **(c)** V_{ti} **- URANS blade-resolved** **(d)** V_{ti} **- RANS/BET with blade-resolved iso-lines**

Fig. 33 Slices of velocity fields half a rotor radius behind the propeller.

explained for axial flows, but computations at different propeller incidence angles led to the same observations. It was also shown that a key parameter to correctly setup a RANS/BET computation is the quantity of source terms placed upstream of the velocity sampling lines that are used for the BET computation. Results show that the only way to verify fundamental Blade Element Momentum Theory results is to distribute half of the source terms upstream of the velocity sampling lines, and the other half downstream. This is in agreement with what was done in previous work without proper justification. As a result, any density function can be used to distribute the source terms in the axial direction, as long as the distribution is balanced on both sides of the sampling lines.

Because the RANS/BET approach averages the propeller loads over a whole revolution like an actuator disk, it does not model tip vortices. The need for a tip-loss correction was explained and four formulations were tested. The one that performed the best is a Glauert correction of the induced velocities combined with a loads correction calibrated on a blade-resolved case. The proposed correction is specific to the studied propeller, but it was shown to be resilient to a change of operating point. Future work could include developing a calibrated induced velocities correction, which would lead to a better prediction of propeller efficiency.

The RANS/BET model was evaluated for a wide range of pitch angles in axial flow and the obtained propeller characteristics were in good agreement with the RANS and URANS blade-resolved simulations. This shows that the tip-loss correction that was calibrated on a specific operating point is also valid for other pitch angles. Likewise, the RANS/BET model was tested for propeller incidence angles of 3°, 6°, and 9° to evaluate its capacity to predict non-axial flows. The propeller performance was slightly less accurate than without incidence, but the loads distribution and the velocity fields in the wake were remarkably well predicted compared to RANS and URANS blade-resolved computations.

All the work presented in this paper focused on building a model capable of predicting the loads and flow field accurately compared to a RANS and URANS blade-resolved computation, for a propeller at a given pitch angle. For

pre-design analyses, the body force models are always trimmed to target a given thrust. Future work will include trimming the developed model to match CFD blade-resolved thrust and evaluate how accurately the flow field can be predicted. The work done on source term distribution will also be used to develop an actuator line model capable of predicting unsteady propeller wakes.

Acknowledgements

This project has received funding from the Clean Sky 2 Joint Undertaking (JU) under grant agreement No 945583. The JU receives support from the European Union's Horizon 2020 research and innovation programme and the Clean Sky 2 JU members other than the Union. The results, opinions, conclusions, etc. presented in this work are those of the author(s) only and do not necessarily represent the position of the JU; the JU is not responsible for any use made of the information contained herein.

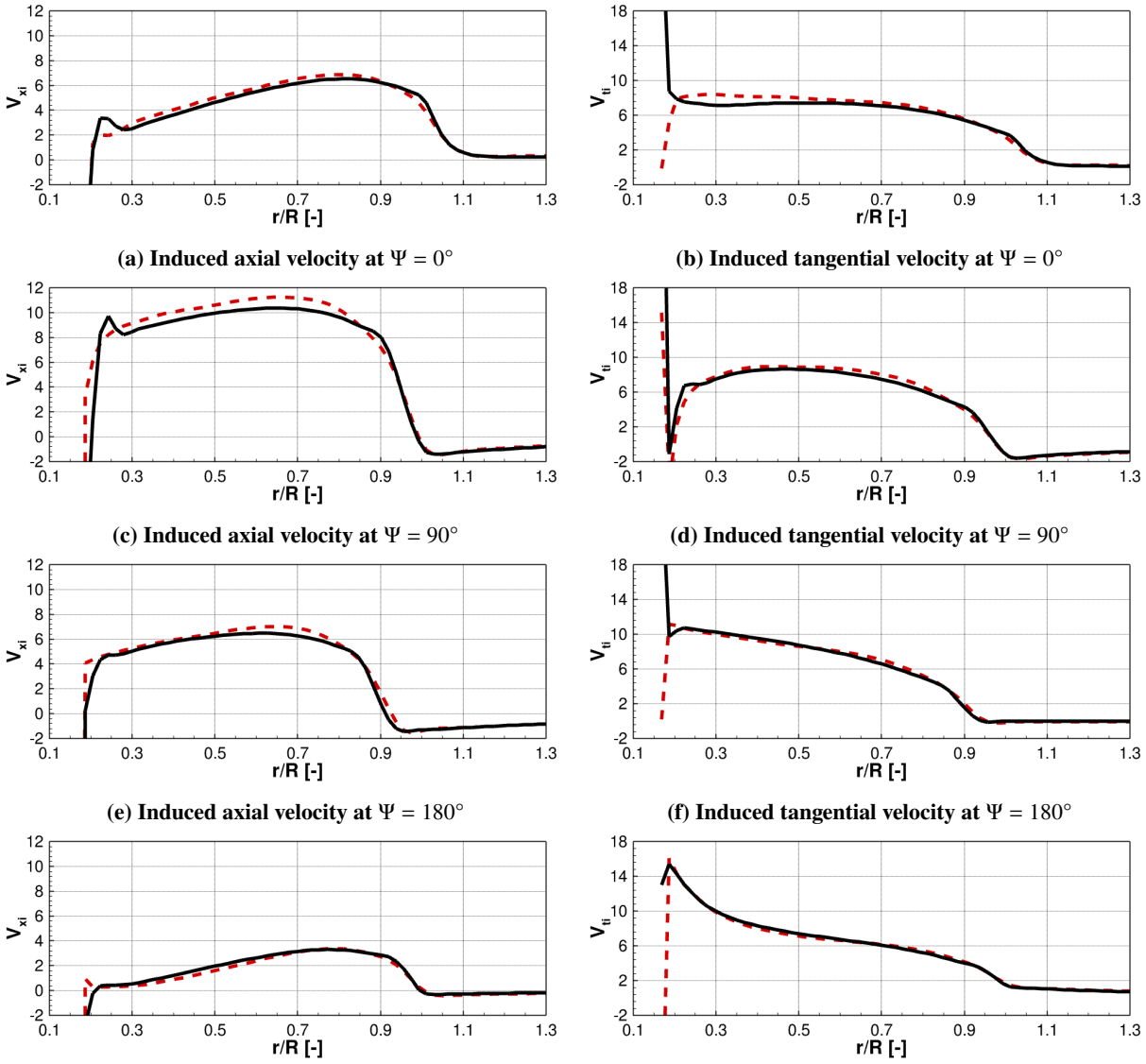

(a) Induced axial velocity at Ψ = 0°

(b) Induced tangential velocity at Ψ = 0°

(c) Induced axial velocity at Ψ = 90°

(d) Induced tangential velocity at Ψ = 90°

(e) Induced axial velocity at Ψ = 180°

(f) Induced tangential velocity at Ψ = 180°

(g) Induced axial velocity at Ψ = 270°

(h) Induced tangential velocity at Ψ = 270°

URANS blade-resolved (——), RANS/BET (- - -)

Fig. 34 Profiles of induced velocities half a propeller radius behind the rotor at different azimuth angles Ψ.

References

[1] Glauert, H., "Airplane Propellers," *Aerodynamic Theory*, Vol. IV, edited by W. F. Durand, Springer, Berlin, Heidelberg, 1935, pp. 169–360.

[2] Prandtl, L., "Applications of Modern Hydrodynamics to Aeronautics," Tech. Rep. NACA-TR-116, Jan. 1923.

[3] Sørensen, J., and Shen, W. Z., "Numerical Modeling of Wind Turbine Wakes," *Journal of Fluids Engineering*, Vol. 124, No. 2, 2002, pp. 393–399. https://doi.org/10.1115/1.1471361.

[4] Fejtek, I., and Roberts, L., "Navier-Stokes computation of wing/rotor interaction for a tilt rotor in hover," *AIAA Journal*, Vol. 30, No. 11, 1992, pp. 2595–2603. https://doi.org/10.2514/3.11272.

[5] Moens, F., and Gardarein, P., "Numerical simulation of the propeller/wing interactions for transport aircraft," *19th AIAA Applied Aerodynamics Conference*, American Institute of Aeronautics and Astronautics, 2001. https://doi.org/10.2514/6.2001-2404.

[6] Rajagopalan, R. G., and Lim, C. K., "Laminar Flow Analysis of a Rotor in Hover," *Journal of the American Helicopter Society*, Vol. 36, No. 1, 1991, pp. 12–23. https://doi.org/10.4050/JAHS.36.1.12.

[7] Rajagopalan, R. G., and Mathur, S. R., "Three Dimensional Analysis of a Rotor in Forward Flight," *Journal of the American Helicopter Society*, Vol. 38, No. 3, 1993, pp. 14–25. https://doi.org/10.4050/JAHS.38.14.

[8] Zori, L. A. J., and Rajagopalan, R. G., "Navier—Stokes Calculations of Rotor—Airframe Interaction in Forward Flight," *Journal of the American Helicopter Society*, Vol. 40, No. 2, 1995, pp. 57–67. https://doi.org/10.4050/JAHS.40.57.

[9] Sørensen, J. N., and Myken, A., "Unsteady actuator disc model for horizontal axis wind turbines," *Journal of Wind Engineering and Industrial Aerodynamics*, Vol. 39, No. 1, 1992, pp. 139–149. https://doi.org/10.1016/0167-6105(92)90540-Q.

[10] Sørensen, J. N., Shen, W. Z., and Munduate, X., "Analysis of wake states by a full-field actuator disc model," *Wind Energy*, Vol. 1, No. 2, 1998, pp. 73–88. https://doi.org/10.1002/(SICI)1099-1824(199812)1:2<73::AID-WE12>3.0.CO;2-L.

[11] Mikkelsen, R., Sørensen, J. N., and Shen, W. Z., "Modelling and analysis of the flow field around a coned rotor," *Wind Energy*, Vol. 4, No. 3, 2001, pp. 121–135. https://doi.org/10.1002/we.50.

[12] Martinez, L., Leonardi, S., Churchfield, M., and Moriarty, P., "A Comparison of Actuator Disk and Actuator Line Wind Turbine Models and Best Practices for Their Use," *50th AIAA Aerospace Sciences Meeting including the New Horizons Forum and Aerospace Exposition*, American Institute of Aeronautics and Astronautics, 2012. https://doi.org/10.2514/6.2012-900.

[13] Stokkermans, T. C. A., van Arnhem, N., Sinnige, T., and Veldhuis, L. L. M., "Validation and Comparison of RANS Propeller Modeling Methods for Tip-Mounted Applications," *AIAA Journal*, Vol. 57, No. 2, 2019, pp. 566–580. https://doi.org/10.2514/1.J057398.

[14] Zhong, W., Wang, T. G., Zhu, W. J., and Shen, W. Z., "Evaluation of Tip Loss Corrections to AD/NS Simulations of Wind Turbine Aerodynamic Performance," *Applied Sciences*, Vol. 9, No. 22, 2019, p. 4919. https://doi.org/10.3390/app9224919.

[15] Ortun, B., "A coupled RANS/lifting-line analysis for modelling the aerodynamics of distributed propulsion," AHS Technical Conference on Aeromechanics Design for Transformative Vertical Flight, San Francisco, CA, 2018.

[16] Reboul, G., Lewis, D., Balmaseda, M., Bailly, J., Falissard, F., Guntzer, F., and Lienard, C., "Multi-fidelity Aeroacoustic Prediction of an eVTOL Rotor," *Vertical Flight Society's 79th Annual Forum and Technology Display*, West Palm Beach, FL, 2023.

[17] Betz, A., "Schraubenpropeller mit geringstem Energieverlust. Mit einem Zusatz von l. Prandtl," *Nachrichten von der Gesellschaft der Wissenschaften zu Göttingen, Mathematisch-Physikalische Klasse*, 1919, pp. 193–217.

[18] Wilson, R. E., and Lissaman, P. B. S., *Applied Aerodynamics of Wind Power Machines*, NTIS, 1974.

[19] Wilson, R. E., Lissaman, P. B. S., and Walker, S. N., "Aerodynamic performance of wind turbines," Tech. Rep. PB-259089, Oregon State University, 1976.

[20] De Vries, O., "Fluid Dynamic Aspects of Wind Energy Conversion," Tech. rep., AGARD, Jul. 1979.

[21] Shen, W. Z., Mikkelsen, R., Sørensen, J. N., and Bak, C., "Tip Loss Corrections for Wind Turbine Computations," *Wind Energy*, Vol. 8, No. 4, 2005, pp. 457–475. https://doi.org/10.1002/we.153.

[22] Sørensen, J. N., and Kock, C. W., "A model for unsteady rotor aerodynamics," *Journal of Wind Engineering and Industrial Aerodynamics*, Vol. 58, No. 3, 1995, pp. 259–275. https://doi.org/10.1016/0167-6105(95)00027-5.

[23] Shen, W. Z., Sørensen, J. N., and Mikkelsen, R., "Tip Loss Correction for Actuator/Navier–Stokes Computations," *Journal of Solar Energy Engineering*, Vol. 127, No. 2, 2005, pp. 209–213. https://doi.org/10.1115/1.1850488.

[24] Adkins, C., and Liebeck, R., "Design of optimum propellers," *Journal of Propulsion and Power*, Vol. 10, No. 5, 1983.

[25] Borer, N. K., Moore, M. D., and Turnbull, A., "Tradespace Exploration of Distributed Propulsors for Advanced On-Demand Mobility Concepts," *14th AIAA Aviation Technology, Integration, and Operations Conference*, American Institute of Aeronautics and Astronautics, 2014. https://doi.org/10.2514/6.2014-2850.

[26] Cambier, L., Heib, S., and Plot, S., "The Onera elsA CFD software: input from research and feedback from industry," *Mechanics & Industry*, Vol. 14, No. 3, 2013, pp. 159–174. https://doi.org/10.1051/meca/2013056.

[27] Jameson, A., Schmidt, W., and Turkel, E., "Numerical Solution of the Euler Equations by Finite Volume Methods Using Runge-Kutta Time Stepping Schemes," *AIAA Paper*, 1981. https://doi.org/10.2514/6.1981-1259.

[28] Martinelli, L., and Jameson, A., "Validation of a multigrid method for the Reynolds averaged equations," *26th Aerospace Sciences Meeting*, American Institute of Aeronautics and Astronautics, 1988. https://doi.org/10.2514/6.1988-414.

[29] Kok, J. C., "Resolving the Dependence on Freestream Values for the k- Turbulence Model," *AIAA Journal*, Vol. 38, No. 7, 2000, pp. 1292–1295. https://doi.org/10.2514/2.1101.

[30] Menter, F. R., "Two-equation eddy-viscosity turbulence models for engineering applications," *AIAA Journal*, Vol. 32, No. 8, 1994, pp. 1598–1605. https://doi.org/10.2514/3.12149.

[31] Zheng, Z., and Liu, F., "Staggered upwind method for solving Navier-Stokes and k- omega turbulence model equations," *AIAA Journal*, Vol. 33, 1995, pp. 991–998. https://doi.org/10.2514/3.12808.

[32] Mudry, M., "La théorie générale des nappes et filaments tourbillonaires et ses applications à l'aérodynamique instationnaire," PhD Thesis, Université Pierre et Marie Curie - Paris VI, 1982.

[33] Ben Nasr, N., Falissard, F., Decours, J., Gaveriaux, R., Delrieux, Y., Canard-Caruana, S., Laban, M., Brouwer, H., Albreicht, M., Scholz, C., Diette, C., and Chartrain, D., "Propeller Analysis Using Low & High Fidelity Aero-acoustic Methods," *35th AIAA Applied Aerodynamics Conference*, American Institute of Aeronautics and Astronautics, 2017. https://doi.org/10.2514/6.2017-3573.

[34] Blondel, F., Boisard, R., Milekovic, M., Ferrer, G., Lienard, C., and Teixeira, D., "Validation and comparison of aerodynamic modelling approaches for wind turbines," *Journal of Physics: Conference Series*, 2016. https://doi.org/10.1088/1742-6596/753/2/022029.

[35] Boisard, R., "Numerical Analysis of Rotor/Propeller Aerodynamic Interactions on a High-Speed Compound Helicopter," *Journal of the American Helicopter Society*, Vol. 67, No. 1, 2022, pp. 1–15. https://doi.org/10.4050/JAHS.67.012005.

[36] Lienard, C., Boisard, R., and Daudin, C., "Aerodynamic Behavior of a Floating Offshore Wind Turbine," *AIAA Journal*, Vol. 58, No. 9, 2020, pp. 3835–3847. https://doi.org/10.2514/1.J059255.

[37] Gong, Y., Tan, C. S., Gordon, K. A., and Greitzer, E. M., "A Computational Model for Short-Wavelength Stall Inception and Development in Multistage Compressors," *Journal of Turbomachinery*, Vol. 121, No. 4, 1999, pp. 726–734. https://doi.org/10.1115/1.2836726.

[38] Hall, D. K., Greitzer, E. M., and Tan, C. S., "Analysis of Fan Stage Conceptual Design Attributes for Boundary Layer Ingestion," *Journal of Turbomachinery*, Vol. 139, No. 7, 2017. https://doi.org/10.1115/1.4035631.

[39] Thollet, W., Dufour, G., Carbonneau, X., and Blanc, F., "Body-force modeling for aerodynamic analysis of air intake – fan interactions," *International Journal of Numerical Methods for Heat & Fluid Flow*, Vol. 26, No. 7, 2016, pp. 2048–2065. https://doi.org/10.1108/HFF-07-2015-0274.

[40] Cao, T., Hield, P., and Tucker, P. G., "Hierarchical Immersed Boundary Method with Smeared Geometry," *Journal of Propulsion and Power*, Vol. 33, No. 5, 2017, pp. 1151–1163. https://doi.org/10.2514/1.B36190.

[41] Rankine, W., "On the Mechanical Principles of the Action of Propellers," *Transactions of the Institution of Naval Architects*, Vol. 6, 1865.

[42] Froude, W., "On the Elementary Relation Between Pitch, Slip, and Propulsive Efficiency," Tech. Rep. NACA-TM-1, 1878.